From spikes to intercellular waves: tuning the strength of calcium stimulation modulates organ size control

Ramezan Paravitorghabeh[a,1], **Dharsan Soundarrajan**[a,2], **and Jeremiah J. Zartman**[a,3]

[a]Department of Chemical and Biomolecular Engineering, University of Notre Dame, Notre Dame, IN, USA

Calcium (Ca^{2+}) signaling is a fundamental molecular communication mechanism for the propagation of information in eukaryotic cells. Cytosolic calcium ions integrate a broad range of hormonal, mechanical and electrical stimuli within cells to modulate downstream cellular processes involved in organ development. However, how the spatiotemporal dynamics of calcium signaling are controlled at the organ level remains poorly understood. Here, we show that the spatiotemporal extent of calcium signaling within an epithelial system is determined by the class and level of hormonal stimulation and by the subdivision of the cell population into a small fraction of initiator cells surrounded by a larger fraction of standby cells connected through gap junction communication. To do so, we built a geometrically accurate computational model of intercellular Ca^{2+} signaling that spontaneously occurs within developing *Drosophila* wing imaginal discs. The multi-scale computational model predicts the regulation of the main classes of Ca^{2+} signaling dynamics observed in vivo: single cell Ca^{2+} spikes, intercellular transient bursts, intercellular waves and global fluttering. We show that the tuning of the spatial extent of Ca^{2+} dynamics from single cells to global waves emerges naturally as a function of global hormonal stimulation strength. Further, this model provides insight into how emergent properties of intercellular calcium signaling dynamics modulates cell growth within the tissue context. It provides a framework for analyzing second messenger dynamics in multicellular systems.

Ca^{2+} signaling | Second messengers | Gap junction communication | Spatiotemporal patterns | Information processing | Hopf bifurcation.

Calcium ions (Ca^{2+}) mediate a large number of physiological and regulatory processes such as proliferation, differentiation, transcription, metabolism, cellular motility, fertilization, neuronal communication, muscle contraction, wound healing, cellular senescence and apoptosis (1–10). Such a broad range of functionality is primarily induced through coordinated variations in cytosolic free Ca^{2+} concentration in space and time (11). In addition to modulating cellular processes, Ca^{2+} signaling also regulates developmental processes at the multicellular level. For instance, Ca^{2+} is shown to regulate scale development in the butterfly (12) and mediates autophagic and apoptotic processes required for hearing acquisition in the developing cochlea (13, 14). A major challenge for understanding the emergent properties of Ca^{2+} signaling in multicellular systems is the lack of a suitable framework for analyzing, imaging and perturbing the stochastic signals systematically.

In our recent study, we found that Ca^{2+} dynamics correlates with final organ size during the development of the *Drosophila* larval wing disc, a genetic model for organogenesis (15). Specifically, Ca^{2+} dynamics in growing wing discs exhibit a progression from a global "fluttering" state in smaller, younger discs to infrequent single cell spikes in large, older discs as development proceeds. This ordinal progression is recapitulated by culturing ex vivo cultured wing discs with increasing concentrations of fly extract (FEX) titration, a serum-based stimulus of calcium activity. However, it remains unclear what might govern this progression mechanistically. This is important for decoding calcium signaling in developmental systems.

A major challenge in deciphering spontaneous calcium activity in tissues is the lack of computational models to quantify the multiplexed dynamics of the multiple regulators of Ca^{2+} activity in multicellular systems. Here, we have overcome this bottleneck by developing and validating a multi-scale model of Ca^{2+} signaling pathway that identifies the key parameters that determine transitions between tissue-wide calcium phenomena. This computational model provides key predictions on the underlying biophysical spatiotemporal patterning of parameters shaping calcium signaling dynamics needed to recapitulate the qualitative modes of calcium signaling dynamics that occur in epithelial systems: cellular Ca^{2+} spikes, multicellular transients, Ca^{2+} waves, or the global fluttering state (Fig. 1).

A second question in the field is how these different spatiotemporal modes of Ca^{2+} signaling impact downstream cellular or developmental processes. Here, we provide experimental evidence that local intercellular Ca^{2+} transients are linked to insulin signaling that directs promotion of tissue growth. In contrast, promotion of intercellular Ca^{2+} waves through overexpression of the $G\alpha_q$ subunit reduces wing size. Together

---

Significance Statement

Intercellular calcium signaling is critical for epithelial morphogenesis and homeostasis. However, how cytosolic calcium concentration dynamics are regulated at the multicellular level are poorly understood. Here, we show using a novel multiscale computational model that the spatial extent of intercellular calcium communication is controlled by two factors: i) the relative strength of global hormonal stimulation, and ii) the presence of a subset of "initiator cells" among a population of "standby cells" that are connected by gap junctions. Localized multicellular calcium signals are associated with maximal organ growth while persistent calcium waves inhibit overall organ growth. This mechanism explains the broad range of spatiotemporal calcium signaling dynamics that occurs during epithelial development.

The experimental data is imaged by Dharsan Soundarrajan[2].

The authors declare no conflict of interest.

[3]To whom correspondence should be addressed. E-mail: jzartman@nd.edu
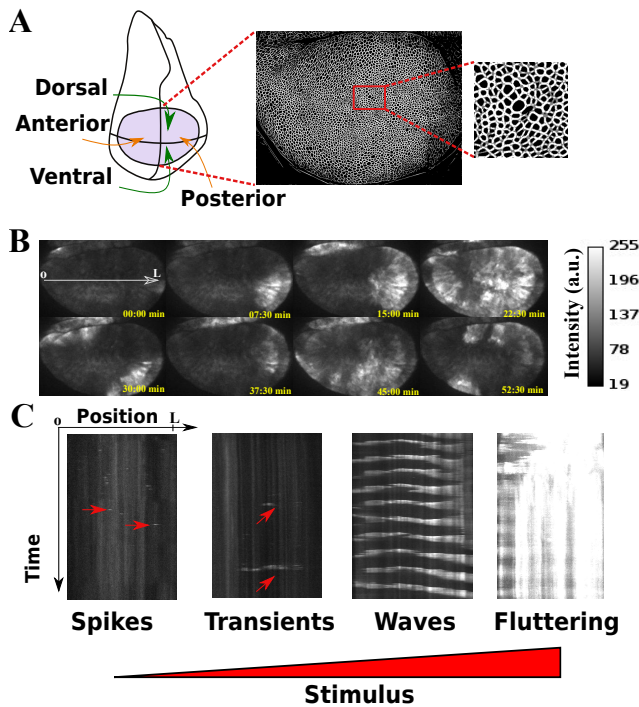
A

B

C

Fig. 1. Four classes of spatiotemporal patterning of Ca^{2+} signaling dynamics in the wing imaginal disc (A) Schematic of wing disc structure with the shaded pouch region defining the region of interest for the present study. (B) Time lapse of intercellular Ca^{2+} waves. (C) Ordinal progression of Ca^{2+} dynamics by increasing stimuli. Kymographs corresponding to Ca^{2+} spikes, intercellular Ca^{2+} transients (ICTs), intercellular Ca^{2+} waves (ICWs) and global fluttering. The red arrows indicate Ca^{2+} activity.

these results support a novel model that links tissue-level calcium signaling dynamics to overall organ size regulation, which we term the "IP$_3$/Ca^{2+} shunt" model. This hypothesis views Ca^{2+} signaling as a readout of two physiological states: stimulation of calcium signaling can be either growth promoting or growth inhibiting depending on the overall net level of stimulated calcium activity. In this model, limited levels of stimulation, leading to localized cellular spikes and limited intercellular calcium transients, provide a readout of growth stimulation. However, high levels of Gα$_q$/Phospholipase C activity are proposed to deplete PIP$_2$ levels (16). This is likely due to substrate depletion of Phosphatidylinositol 4,5-bisphosphate PIP$_2$ through promotion of IP$_3$ generation and downstream Ca^{2+} activity by stimulation of Phospholipase C (PLC) activity. In turn, this would lead to reduced availability of PIP$_2$ for conversion of PIP$_2$ to Phosphatidylinositol-trisphosphate (PIP$_3$), a key second messenger for stimulating protein kinase AKT and downstream growth promotion (17).

In this study, the *Drosophila* 3rd larval instar wing imaginal disc was used as a model platform to investigate the mechanisms governing Ca^{2+} signaling dynamics in epithelia. Fig. 1 summarizes the the experimental system and data. Different classes of patterns emerge at the tissue-level as the level of global stimulation increases: Ca^{2+} spikes, intercellular calcium transients (ICTs), intercellular calcium waves (ICWs) and global fluttering (15). However, a mechanistic understanding linking hormonal stimulation levels to transitions in these qualitative classes of organ-level signaling remains a key question.

Here, we took a hierarchical modeling approach to recapitulate classes of spatiotemporal Ca^{2+} patterns. At the cellular level, we first extended a Ca^{2+} signaling model described in (18) (refer to Fig. 2 for a summary) and modified the activation rate of IP$_3$ receptors to match the experimental data. This new modification of the model was necessary to match the temporal characteristics of Ca^{2+} oscillations derived from the model with the experimental observations (Fig. S1-S4). Next, a chain of cells (1D-model) connected by gap junctions (GJs) were considered in the model (Fig. S5). This led to the main factors affecting propagation of Ca^{2+} signals were identified through analysis of kymographs. We then built a geometrically accurate 2D-model depicted in Fig. 4 A and identified the circumstances underlying various spatiotemporal Ca^{2+} dynamics. Finally, we validated the model with experiments. This enabled us to map the qualitative classes of Ca^{2+} signaling to functional outcomes of relative tissue growth. Each step in hierarchical modeling approach is briefly described in Material and Methods, while the full description is given in Supporting Information. Finally, we summarize the results and propose a model linking the Ca^{2+} signaling readout to size control.

Results

Accounting for calcium-dependent regulation of oscillation duration is required to explain experimental measurements of calcium dynamics. In this study, we used a system of coupled Ordinary Differential Equations (ODEs) to model the basic Ca^{2+} signaling components (Fig.2A, B, see also associated SI text). The baseline model is adapted from (18). At the single cell level, the experimental Ca^{2+} signals in the wing imaginal discs exhibited much longer periods and width at half maximum (WHM) compared to the original model of (18). To match the experimental data, we modified the dynamical equation of r as highlighted in Fig. 2 B. The variable r encodes the rate at which the IP$_3$ receptors can be activated by Ca^{2+}. The proposed dynamical equation is given by

$$\frac{dr}{dt} = \frac{1}{\tau_{max}} \frac{k_\tau^4 + c^4}{k_\tau^4}\Big(1 - r\frac{K_i + c}{K_i}\Big),$$

where in comparison to the original model of (18), the time scale of r is modulated by Ca^{2+}. The modification was necessary to match the temporal characteristics of the model with the experimental data. This modification enables simultaneous control over the frequency (by tuning τ_{max}) and WHM (by tuning k_τ) of Ca^{2+} oscillations. Fig. 2 C, D summarizes the main features of the calibrated model. This suggests that Ca^{2+} can self-regulate frequency and WHM of its oscillations by modulating the activation rate of IP$_3$ receptors. Additional characteristics of the model are described in supporting information Fig. S2, S3. A similar correction (modifying dynamics of r by modulating the corresponding time scale with Ca^{2+}) with an emphasis on frequency calibration of Ca^{2+} signals is reported in (19). However, the underling dynamical equations for modeling Ca^{2+} signaling reported there were slightly different. Specifically, in our model IP$_3$ is described by a Ca^{2+} (and agonist) dependent ODE, while in their model IP$_3$ is a pulse function.

In the single cell model, V_{PLC} encodes the maximum production rate of IP$_3$ (refer to IP$_3$ dynamics in Fig. 2B). V_{PLC} is a Hopf bifurcation parameter. Consequently, if V_{PLC} is above a critical threshold value ($V_{PLC}^* = 0.78$), Ca^{2+} oscillations arise
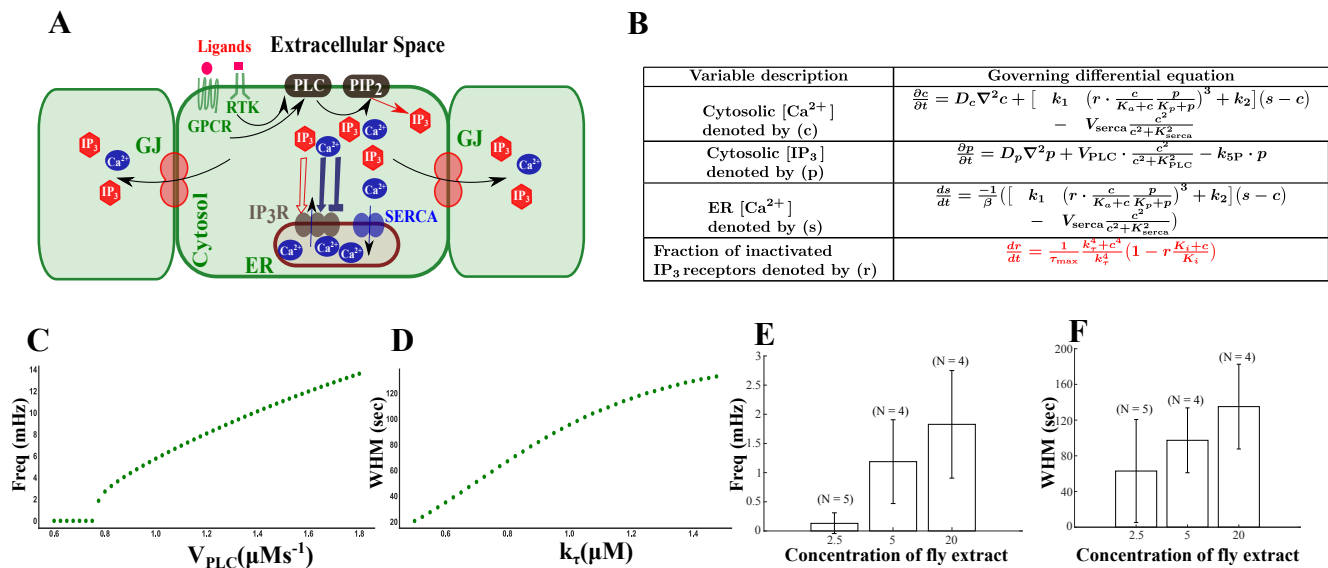
Paravitorghabeh *et al.*

Fig. 2. A modified computational model of calcium signaling captures key signatures of hormone-stimulated calcium transients (A) Major components of Ca^{2+} toolkit; G protein–coupled receptors (GPCR), receptor tyrosine kinase (RTK), gap junctions (GJ), Inositol trisphosphate (IP_3), diacylglycerol (DAG), Phospholipase C (PLC), Phosphatidylinositol 4,5-bisphosphate (PIP_2), sarco/endoplasmic reticulum Ca^{2+}-ATPase (SERCA) and IP_3 receptors (IP_3 R). (B) The summary of baseline Ca^{2+} signaling model adapted from (18). The variables are concentration of cytosolic Ca^{2+}, concentration of IP_3, concentration of Ca^{2+} in Endoplasmic Reticulum (ER), and the fraction of IP_3 receptors that has not been deactivated by Ca^{2+}. The permeability of Ca^{2+} and IP_3 are denoted by D_c and D_p, respectively. More details on each dynamical equation and meaning of the parameters in the model are described in Supporting Information. The nominal values are summarized in Table S1. (C) Increasing V_{PLC} in the model increases frequency of oscillations in a single cell ($D_c = D_p = 0$). This effect is similar to the original model (18). (D) Increasing k_τ increases width at half maximum (WHM) of the Ca^{2+} oscillations in a single cell ($D_c = D_p = 0$). For this simulation, $V_{PLC} = 1.2$ is fixed, and k_τ is varied. (E) Increasing the concentration of fly extract, a chemical stimulus of calcium signaling, increases the overall frequency of Ca^{2+} oscillations in the wing disc. Frequencies of Ca^{2+} dynamics from all the cells in the wing discs are averaged. and (F) Increasing the concentration of fly extract increases the overall width of half max (WHM) of Ca^{2+} oscillations. Error bars represent standard deviation.

(refer to Fig. S2). Otherwise, the Ca^{2+} levels remains at its rest value (basal level), and oscillations do not occur. Therefore, V_{PLC} is considered the parameter that encodes the chemical stimulus (FEX) for the simulations.

To study the behavior of Ca^{2+} signaling in coupled cells, we first considered a simplified model consisting of a chain of cells connected by gap junctions (GJs). The details of the $1D$ model are described in Supporting Information, and insights are summarized below. The $1D$ model demonstrates that when V_{PLC} is below V^*_{PLC}, but very close to it, a small amount of diffusive IP_3 can trigger Ca^{2+} spikes (refer to Fig. S11). Furthermore, the diffusive IP_3 should have enough strength (defined in terms of energy of diffusive IP_3 signal) to trigger Ca^{2+} signaling (refer to Fig. S12). This observation reveals that when V_{PLC} is close to the Hopf bifurcation threshold, cells are much more prone to stimulate release of Ca^{2+} from the ER store into the cytosol due to diffusion of IP_3. This important finding leads the way to understand the underlying principles for emergence of Ca^{2+} patterns at the tissue level. Another prediction from the $1D$ model is that when the gap junction permeability is increased, the triggering of Ca^{2+} signals in neighborhood cells occur faster. Therefore, permeability of GJs affect the speed of Ca^{2+} propagation. This is due to the fact that the accumulated IP_3, which diffuses through GJs, is the key for triggering Ca^{2+} release from internal stores (See Supporting Information Fig. S5).

Gap junction communication coordinates and inhibits tissue-level Ca^{2+} signaling activity. Next, we built a geometrically accurate tissue model that consists of a collection of cells connected by GJ's. Each cell has its own dynamical equations describing the Ca^{2+} signaling toolkit with additional terms

corresponding to diffusion of IP_3 and Ca^{2+} (Fig. 2 B). The $2D$ mathematical model suggests that the particular form of tissue-scale Ca^{2+} signaling present in the epithelium depends on two factors: (i) the spatial organization of IP_3 production with respect to the Hopf bifurcation, and (ii) the relative strength of gap junction communication. Here, we provide experimental results to validate key predictions of the model. Throughout the rest of this study, D_p and D_c represent the effective diffusivity of IP_3 and Ca^{2+}, respectively.

Gap junction inhibition in the presence of a stimulus leads to asynchronous Ca^{2+} signaling. Cells exhibit oscillatory Ca^{2+} dynamics with no coordination among them when GJs were blocked in the presence of hormonal stimulation (FEX stimulation, Movies S1-S2). These results demonstrate the main role of gap junction communication is in the coordination of activity of spatiotemporal Ca^{2+} patterns between cells in the tissue. When the gap junctions are not blocked, a diverse range of spatiotemporal patterns emerges in the experimental data (Fig. 1C).

Inhibition of gap junction communication increases Ca^{2+} spikes. The experiment summarized in Fig. 3 provides evidence that reduction of gap junction communication increases Ca^{2+} signaling within individual cells under low levels of stimulation. Specifically, both control and test discs were cultured without using any external chemical stimulus such as FEX. The control shows almost no Ca^{2+} activity (Fig. 3A). However, when gap junction communication is blocked in the tissue, Ca^{2+} spikes appear (Fig. 3B). Fig. 3C represents the simulation results to recapitulate the transition from no Ca^{2+} activity to the emergence of spikes by decreasing gap junction permeability.
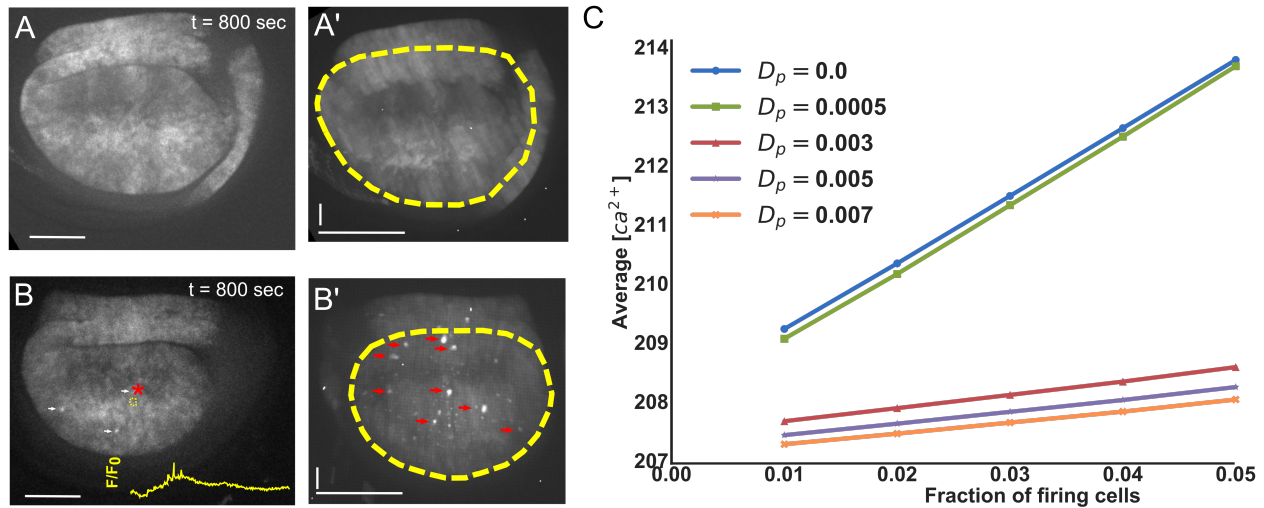
Fig. 3. Gap junction communication decreases Ca²⁺ spikes in the wing disc cells. A-B) Montages from ex vivo time-lapse movies of *nub>GCaMP6f × UAS-RyR^RNAi* (control) wing discs. A) Wing discs were imaged in Grace's low ecdysone media for 1 hr at 10 sec intervals [20]. Under this condition, we observed no Ca²⁺ activity in the wing disc cells. A') t-projection of the time lapse stack. The wing disc boundary is indicated with the yellow dashed line. B) Gap junction communication was blocked by culturing wing discs in Grace's low ecdysone media with $100mM$ of Carbenoxolone (Cbx). We observed a significant number of Ca²⁺ spikes in the 1 hr time interval when GJs were inhibited. B') t-projection of the time lapse movies. Yellow dotted lines indicated disc boundary. Scale bar refers to $100\mu m$ respectively. (C) Simulation result to identify the transition from no Ca²⁺ activity to spikes. For this simulation, most of the the cells have V_{PLC} below the Hopf threshold (no stimulation), while a tiny fraction of cells (x-axis) are slightly above the Hopf threshold ($V_{\text{PLC}} = 0.8$). Then, the average Ca²⁺ levels over the tissue under variable gap junction permeability was computed. When GJs are blocked ($D_p = 0$), the average Ca²⁺ levels of the tissue are higher. This increase is due to stimulation of cellular Ca²⁺ spikes. When D_p is increased, the Ca²⁺ levels drop to basal level. For all cases, $D_c = 0.1D_p$ [21]. The units of average Ca²⁺ concentration is μM.Horizontal scale bars in A,A',B,B' represent 100 μm and the vertical scale bar in A' and B' represent 6 min. Montages in A' and B' were slightly adjusted for brightness and contrast for clarity.

Most of the cells have V_{PLC} below the Hopf bifurcation threshold to simulate no external stimulus, except a tiny fraction of cells that have V_{PLC} slightly greater than the bifurcation threshold. We then varied the gap junction permeability and computed the average Ca²⁺ levels over the tissue by computing the average integrated Ca²⁺ levels

$$\frac{1}{N}\sum_{i=1}^{N}\int_0^T c_i(t)dt.$$

189 Here, N is the total number of cells in the tissue, T is the
190 simulation period (1 hour), and $c_i(t)$ is the Ca²⁺ signal for
191 individual cells. When gap junctions are blocked, the average
192 Ca²⁺ levels are higher. This increase is due to the occurrence
193 of spontaneous Ca²⁺ spikes (Fig. 3C). When gap junctions are
194 blocked, the IP₃ produced in those cells, which are set to be
195 slightly above the bifurcation threshold triggers Ca²⁺ spikes
196 (there is no diffusion of IP₃ to neighboring cells). When gap
197 junctions are open, the produced IP₃ diffuses to neighboring
198 cells, and no Ca²⁺ spike can be triggered (due to insufficient
199 accumulation of IP₃). Thus, gap junction communication
200 effectively raises the threshold needed for significant release
201 of Ca²⁺ into the cytosol. This suggests that gap junction
202 communication acts to 'inhibit' calcium signaling. Below,
203 we discuss the necessary conditions for the main classes of
204 Ca²⁺ patterns in the presence of a stimulus.

205 ***The distribution of V_{PLC} with respect to the Hopf bifurcation***
206 ***governs transitions between spatiotemporal classes of tis-***
207 ***sue-level signaling dynamics.*** In experimental data Fig. 1 C,
208 different tissue-level patterns of Ca²⁺ signaling are observed.
209 The main classes include (i) Ca²⁺ local spikes, (ii) intercellular

Ca²⁺ transients (ICTs), (iii) intercellular Ca²⁺ waves (ICWs), 210
and (iv) global fluttering in ordinal progression by increasing 211
stimulus. The first three classes have a common feature: a 212
small fraction of cells in the tissue that serve as initiation sites 213
for the onset of Ca²⁺ signals. However, in the global fluttering 214
mode, most of the cells in the disc are in active state. Fig. 4 215
D-G summarizes the simulation results for spikes, ICTs, ICWs 216
and global fluttering (also refer to SI simulation movies S4, 217
S6, S8, S13). These results demonstrate that the spatial distri- 218
bution of V_{PLC}, *with respect to the Hopf bifurcation threshold*, 219
is the key factor that determines the specific form of intercel- 220
lular Ca²⁺ signaling. Fig. 4 C illustrates the distribution of 221
V_{PLC}, which leads to either Ca²⁺ spikes, ICTs or ICWs. As 222
the distribution of IP₃ production rates become closer to the 223
Hopf bifurcation threshold, the spatial extent of Ca²⁺ signaling 224
becomes larger. In other words, a subpopulation of initiator 225
cells regulates the range of signal transmission by organizing 226
IP₃ production rate with respect to a Hopf bifurcation and in 227
the presence of gap junction communication. This explains the 228
ordinal progression of Ca²⁺ dynamics observed as the concen- 229
tration of chemical stimulus such as FEX is increased. Fig. 4 230
H shows how Ca²⁺ waves can form based on patterning of 231
maximum production of PLC activity (V_{PLC}). As depicted 232
in Fig. S20, reducing V_{PLC} in a stripe along A/P axis, while 233
keeping the rest of cells near Hopf bifurcation also leads to 234
spiral form of Ca²⁺ waves (refer to SI simulation movie S10). 235
An example of such an experimental observed spiral wave is 236
depicted in the SI movie S9. 237

G$\alpha_{\mathbf{q}}$ overexpression in the absence of stimulus induces 238
Ca²⁺ waves and leads to reduced wing size. To further con- 239
firm our prediction that the position of V_{PLC} with respect 240
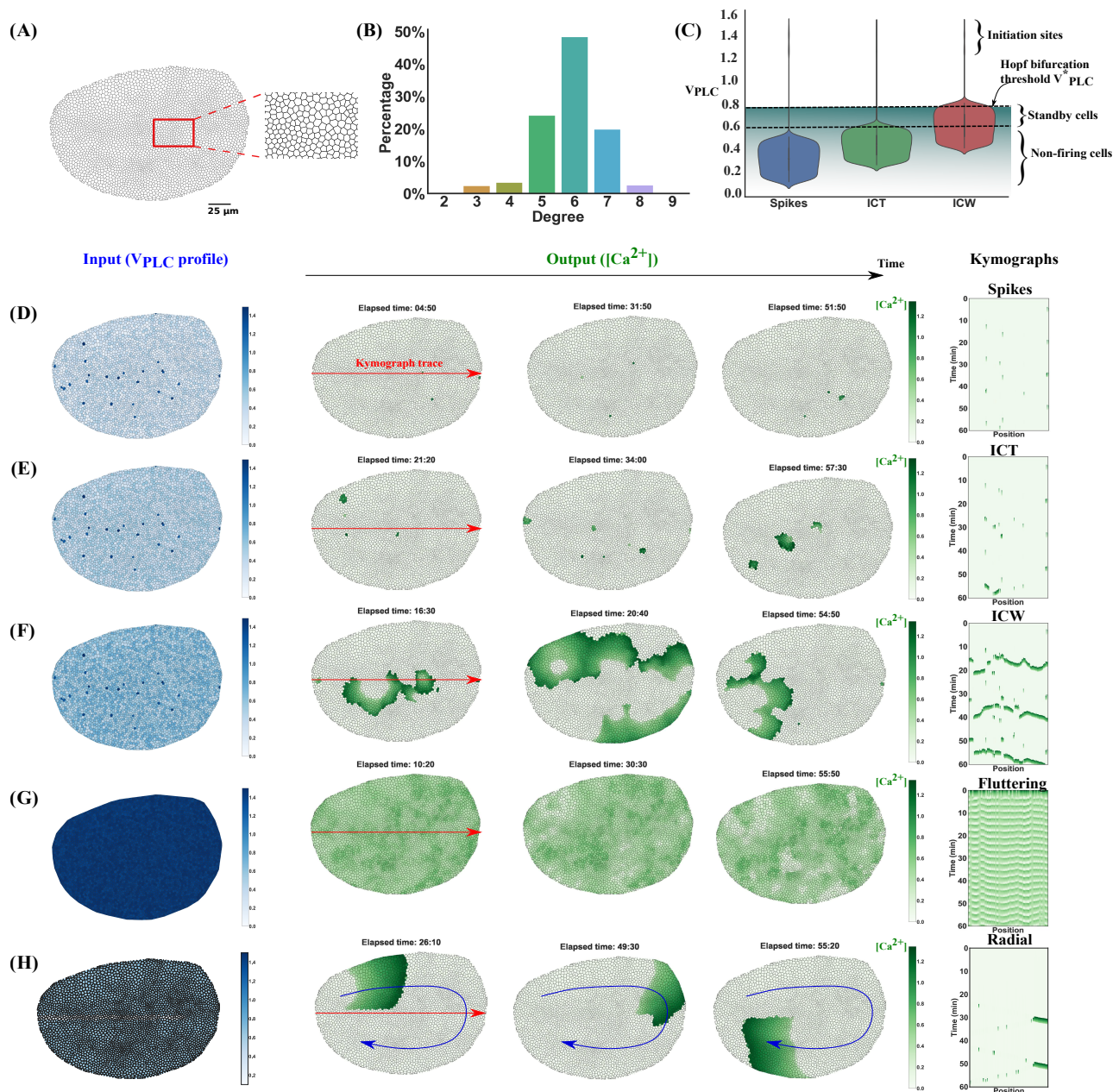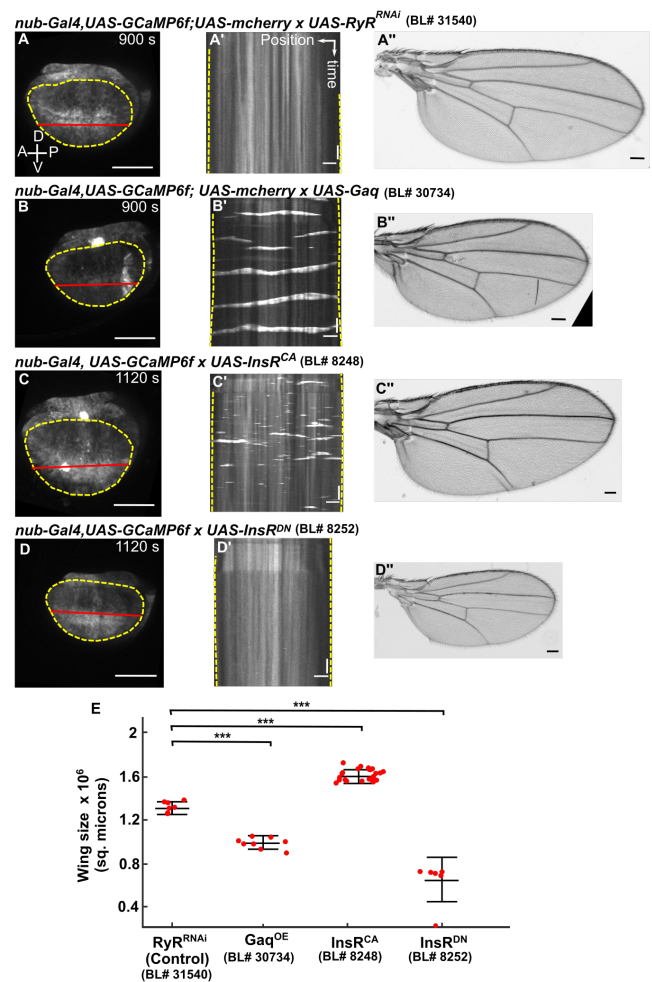
Paravitorghabeh *et al.*

Fig. 4. Tuning global stimulation strength governs the spatial extent of intercellular Ca²⁺ communication. (A) An experimental image of a third instar wing disc served as a template for defining the simulated tissue. In brief, cells were segmented from a wing disc. Centroids of segmented cells were used to define cellular positions in the simulated wing disc. (B) A Voronoi tesselation followed by multiple rounds of Lloyd's relaxation (22) was used to define a template wing disc that matches the experimentally observed network topology (refer to Fig. 1 (A) for experimental image). For each cell in the tissue the set of ODEs based on the proposed model is solved Fig. 1 B, while neighboring cells exchange Ca²⁺ and IP_3 through GJs. (C) Distribution of V_{PLC} with respect to a Hopf bifurcation for three main classes of Ca²⁺ dynamics. All three classes including local spikes, ICTs and ICWs have a common characteristics: a small fraction of cells with high values of V_{PLC} which are the initiation sites. However, distribution of V_{PLC} in rest of the cells determines the extent of intercellular Ca²⁺signaling: (i) when the majority of cells have V_{PLC} much smaller than V_{PLC}^*, local spikes emerge, (ii) if a significant fraction of cells have low V_{PLC}, but close to V_{PLC}^*, then ICTs emerge, (iii) if most of the cells have V_{PLC} in close vicinity of V_{PLC}^*, then ICWs emerge. Depending on V_{PLC}, each individual cell can be classified as (i) a non-firing cell, which has low levels of IP_3 production (small V_{PLC}) and hinders long-range signal propagation, (ii) a standby cell with V_{PLC} near Hopf bifurcation V_{PLC}^* capable of firing Ca²⁺ signaling by a small amount of diffusive IP_3 and (iii) initiator cells, which exhibit high values of V_{PLC}, likely through an increased receptivity to hormonal signaling. The shaded area in panel (C) highlights the region below the Hopf threshold where the standby and non-firing cells are located. Each row in (D-H) contains the IP_3 production rate profile (V_{PLC} levels for individual cells), three frames corresponding to time lapse of the simulation window (1 hour) and the corresponding kymograph along the red arrow. (D) Individual Ca²⁺ spikes occur when the majority of cells have IP_3 production rates that are very low and away from the Hopf bifurcation threshold. (E) ICTs occur when the majority of cells have IP_3 production rates that are low but close to Hopf bifurcation threshold. (F) ICWs occur when the majority of cells have IP_3 production rates that are in vicinity of Hopf bifurcation threshold. For panel (D-F), the initiation sites are roughly 1% of total number cells and spatially distributed at random throughout the tissue (same random locations for each class). As depicted in leftmost column, while (D), (E) and (F) have small number of initiation sites, the IP_3 production rate in rest of the cells increases gradually. (G) Global fluttering occurs when almost all the cells have high IP_3 production rate and higher values of K_{serca}. (H) Spiral Ca²⁺ waves (along the blue arrow) emerge by carefully chosen V_{PLC} profile. The units for concentration of Ca²⁺are in μM.

to Hopf bifurcation affects the overall Ca^{2+} dynamics, we experimentally tested the effect of overexpressing $G\alpha_q$ on the resulting Ca^{2+} dynamics using the Gal4/UAS system (23, 24). $G\alpha_q$ is one of the subunits of the G-protein that disassociates in response to GPCR activation. Dissociated $G\alpha_q$ activates phospholipase C to convert PIP_2 to DAG and IP_3 (25). Hence, altering the levels of $G\alpha_q$ increases activation of PLCs in the cytosol. We observed the robust formation of intercellular Ca^{2+} waves independent of FEX in the media (Fig. 5B, B'). The waves were periodic in nature and were similar to the FEX-induced waves. We did not observe significant global fluttering or spikes when we overexpressed $G\alpha_q$ in the wing disc. We also observed that overexpression of $G\alpha_q$ resulted in a decrease in the overall size of the wing (Fig. 5 B"). Taken together, our results indicate that the intercellular Ca^{2+} waves is a consequence of $G\alpha_q$ signaling, and that the relative level of stimulated Ca^{2+} signaling activities plays a key role in determining the final size of the adult wing.

Insulin signaling increases wing size but only generates localized Ca^{2+} signals. In addition to FEX, we asked whether other ligands added to the organ culture affects Ca^{2+} activity. In addition to FEX, insulin is added often to organ culture media to stimulate cell proliferation (26, 27). Hence, we asked whether activation of insulin signaling regulates Ca^{2+} activity. Using GAL4/UAS system, we upregulated and downregulated insulin signaling in the wing disc. Strikingly, we observed that activation of insulin signaling results in localized Ca^{2+} spikes and ICTs (Fig. 5 C, C'). However, we did not observe many ICWs. As a second experiment, we varied the concentration of insulin and found that a higher concentration of insulin increased the number of spikes and ICTs. However, we did not see the generation of periodic ICWs. In contrast, no spikes were observed when insulin signaling was inhibited by expressing a dominant negative form of the insulin receptor (Fig. 5 D, D')(28). Furthermore, we did not observe periodic ICWs when insulin signaling was constitutively activated (Fig. 5 C, C')(29). Thus, our results suggest that the localized Ca^{2+} spikes observed ex vivo is activated by insulin signaling. Upregulation of insulin signaling increases the wing size (Fig. 5 C"). Thus, localized Ca^{2+} signal correlates with increased wing size in contrast to global waves in response to GPCR signaling, which correlates with decreased wing size.

Discussion. The main finding of this work is the discovery of a parsimonious explanation that links global hormonal stimulation of calcium signaling to emergent spatiotemporal classes of signaling dynamics (Fig. 6). The model predicts that the distribution of IP_3 production rate with respect to a Hopf bifurcation in the presence of gap junction communication determines the mode of Ca^{2+} signaling in epithelia, and each mode has a specific spatial range. As a consequence, the spatial range of Ca^{2+} signaling can be controlled by tuning tissue level IP_3 production rates. We showed that (i) upregulation of insulin signaling induces localized Ca^{2+} signals with a corresponding increase in final wing size and (ii) $G\alpha_q$ overexpression in the absence of stimulus induces global Ca^{2+} waves and $G\alpha_q$ overexpression leads to reduced wing size,. To elucidate the impact of different modes of Ca^{2+} signaling on tissue growth, the computational model and experimental evidences provide key support for the "IP_3 /Ca^{2+} shunt" hypothesis of tissue size regulation. In this model, tuning IP_3 production lev-

nub-Gal4,UAS-GCaMP6f;UAS-mcherry x UAS-RyR^{RNAi} (BL# 31540)

nub-Gal4,UAS-GCaMP6f; UAS-mcherry x UAS-Gaq (BL# 30734)

nub-Gal4, UAS-GCaMP6f x UAS-InsR^{CA} (BL# 8248)

nub-Gal4,UAS-GCaMP6f x UAS-InsR^{DN} (BL# 8252)

Fig. 5. GPCR and insulin signaling differentially regulates the spatial patterns of Ca^{2+} independent of FEX. A-D) Montages from the ex vivo time-lapse movies, and A'-D') kymographs of the corresponding time-lapse movies. A"-D") Adult wings from the indicated genetic perturbation. In the control wing disc (A-A') cultured in Grace's low 20E media for 1 hr, we did not observe Ca^{2+} waves or Ca^{2+} transients. Overexpression of $G\alpha_q$ in the wing disc (B-B') resulted in the formation of periodic intercellular Ca^{2+} waves. The resulting adult wing from overexpression of $G\alpha_q$ was smaller when compared to controls (A"-B"). Up-regulating insulin signaling in the wing disc (C-C'), which significantly increases wing size, resulted in the formation of Ca^{2+} spikes or Ca^{2+} transients but not waves. Down-regulating insulin signaling in the wing disc (D-D'), which significantly reduces organ size, prevented Ca^{2+} activity in the wing disc (A"-D"). E) Quantification of the adult wing sizes for the indicated genetic perturbations. Scale bars in A-D) and A"-D") represent 100 μm. Horizontal scale bars in A'-D') represent 50 μm. Vertical scale bars in A'-D') represent 6 min. Student t-test was performed. *** $p < 0.001$. Yellow dotted lines indicate pouch boundaries. Red lines indicate xy positions in the kymograph. Labels in E) represent crosses of UAS-*transgene* to parental *nub>GCaMP6f* in the case of InsR^{CA} and InsR^{DN} or *nub>GCaMP6f;mcherry* in the case of RyR^{RNAi} or Gaq. The UAS lines used are UAS RyR^{RNAi} (BL#31540), UAS InsR^{CA} (BL#8248), UAS InsR^{DN} (BL#8252) and UAS Gq (BL#30734) respectively.

els enables control of the common substrate allocation between two different pathways, namely, Ca^{2+} signaling pathway and the PI3K/AKT signaling pathway (16). PIP_2 is the precursor for IP_3 and also modulate PI_3K/AKT pathway (30). If more PIP_2 is allocated for stimulating Ca^{2+} signaling (which induces global Ca^{2+} activity), less PIP_2 is available for PI_3K/AKT pathway (which inhibits the growth). This proposition paves

Paravitorghabeh *et al.*

the way on how to tune one signaling pathway to control another signaling pathway (e.g. PI$_3$K/AKT), which are coupled at the substrate level.

A recent study on signal transmission in a bacterial community suggests that the transition from localized short-range signaling to global community-level communication is associated with a cost-benefit balance (31). In that context, long range signaling increases the overall fitness of the community against chemical attack, while the cost to individual cells is a reduction in growth rate. The proposed model in this work can also be characterized as a cost-benefit trade offs within the context of tissue level Ca^{2+} signaling. For instance, it has been suggested that the fast calcium waves facilitate migration and proliferation of the healing cells by inhibiting excessive apoptotic response during wound healing in epithelia (32). Fig. 6 summarizes the effects of different Ca^{2+} signaling modes in the context of tissue growth and development. Minimal calcium activity, as is observed when insulin signaling is inhibited, correlates with reduced growth, whereas intermediate levels of calcium signaling accompanies strong activation of insulin signaling. However, such signaling does not lead to recurring global calcium waves. GPCR-mediated ICWs lead to a net reduction in tissue growth and therefore are growth inhibiting. Within the context of the "IP$_3$/Ca^{2+} shunt" model, the strong induction of calcium waves will reduce the level of PIP$_2$, a key substrate for growth. This analysis thus motivates future experimental work in this area, which will require careful quantification of PIP$_2$ and PIP$_3$ under genetic perturbations of GPCR signaling. Additionally, future work is needed to quantify the metabolic benefits and costs of calcium signaling during tissue growth.

A possible alternative interpretation would incorporate the coupling of calcium signaling dynamics to tissue growth through cell mechanics. A starting point of the proposed coupling equations can follow the recent proposed model where it was shown that calcium signals and contractions are coupled via a two-way mechanochemical feedback mechanism during apical constriction (33). Finally, a major implication for this work is the translational potential of deliberately shaping calcium signaling activities through spatiotemporally controlled modulation of calcium signaling dynamics in tissues, through a combination of global modulation and local perturbations, to treat or inhibit diseases such as cancer and birth defects.
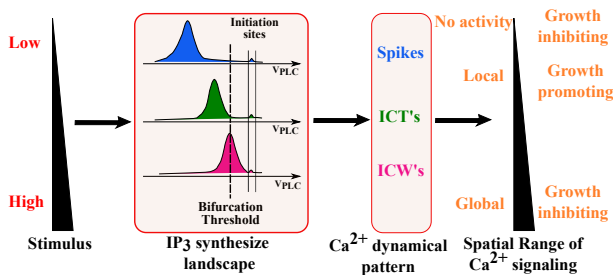

Fig. 6. Summary of key findings based on the proposed model for tissue-level regulation of Ca^{2+} dynamics in epithelial tissues. The spatial range of tissue-level Ca^{2+} signaling is determined by how the IP$_3$ production is organized with respect to a Hopf bifurcation threshold throughout the tissue. Localized Ca^{2+} transients can be associated with insulin-stimulated growth. Global Ca^{2+} signaling inhibits growth.

Materials and Methods

In this study, the *Drosophila* wing imaginal disc in the late larval stages was used as a model platform to investigate the mechanisms governing Ca^{2+} signaling dynamics in epithelia (15, 34, 35). Wing imaginal discs are geometrically simple epithelial organs growing inside the larva. Imaginal discs form different parts of the adult wing and thorax after metamorphosis (36). We restrict the spatial domain of simulations to the wing pouch area, which will form the wing blade, as it is well defined through many genetic studies (see Fig. 1).

Fly stocks. A *nub-GAL4, UAS-GCaMP6f* reporter tester line was created by recombining *nub-GAL4* and *UAS-GCaMP6f* lines (34). Additionally, a second tester line was used that also includes UAS-mcherry. Gene perturbations were generated by crossing the tester line to either RNAi-based transgenic lines (UAS-Gene X^{RNAi}) or gene overexpression (UAS-Gene X). The following UAS transgenic lines were used: UAS-RyR^{RNAi}(BL#31540)(37), UAS-Gq(BL#30734)(38), UAS-InsR^{CA} (BL#8248)(39), UAS-InsR^{DN}(BL#8252)(40). Progeny wing phenotypes are from F1 male progeny emerging form the nub-Gal4, UAS-GCaMP6f/CyO x UAS-X cross or nub-Gal4, UAS-GCaMP6f/CyO; UAS-mcherry x UAS-X cross. Flies were raised at 25C and on a 12-hour light cycle.

Live imaging. Wandering third instar larva approximately 6 days after egg laying were dissected in ZB media with 15% fly extract to obtain wing discs (41). ZB media + 15% fly extract contains 79.4% (v/v) ZB media, 0.6% (v/v) of 1 mg/ml of insulin (Sigma aldrich), 15% ZB-based fly extract and 5% pennicillin/streptomyocin (Gibco). Wing discs were loaded into the previously described REM-Chip (35) and imaged using Nikon Eclipse Ti confocal microscope with a Yokogawa spninning disc and MicroPoint laser ablation system. Image data were collected on an IXonEM+colled CCD camera (Andor technology, South Windsor, CT) using MetaMorph v7.7.9 software (Molecular devices, Sunnyvale, CA). Discs were imaged at three z-planes with a step size of 10 μm, 20x magnification and 10-seconds intervals for a total period of one hour, with 200 ms exposure time, and 50 nW, 488 nm laser exposure at 44 % laser intensity. We blocked gap junction by inhibiting innexin-2 using Carbenoxolone (Cbx, Sigma Aldrich) drug (34). Wing discs were incubated in ZB + 15% FEX with 30 μM Cbx for one hour before imaging. To induce Ca^{2+} transients, we imaged wing discs in ZB media + 2.5 % FEX. Ca^{2+} waves were induced by imaging the wing disc in ZB media + 15% FEX. Ca^{2+} fluttering was observed when discs were imaged in ZB media + 40% FEX respectively.

Quantification of adult wings. Total wing area was measured using imageJ. We traced the wing margin by following veins L1 and L5 and the wing hinge region was excluded from the size analysis.

Intracellular model. A modified model of Ca^{2+} signaling toolkit based on the Politi *et al.* model (18) was utilized in this work. The model is summarized in Fig. 2. A more comprehensive description can be found in Supporting Information. To recapitulate the same time resolution as the experiments, the simulation time is 1 hour and for generating videos, samples are obtained every 10s.

Tissue model. For constructing a realistic model of the tissue, we used experimental images of a wing pouch to build an accurate model of the tissue structure. Fig. 4 A,B depicts the structure of the tissue used for simulations and the statistics of the corresponding network. More detail on the geometry of the model are discussed in Supporting Information.

Intercellular model. The realistic model of the tissue was combined with proposed intracellular model. Diffusion of the second messengers IP$_3$ and Ca^{2+} between adjacent cell was incorporated into the 2D model. Therefore, the tissue level model is a system of coupled ODE's. A complete description of the model is provided in SI materials.

Data availability. All the data and simulation codes are available upon request.

1. Giorgi C, Danese A, Missiroli S, Patergnani S, Pinton P (2018) Calcium dynamics as a machine for decoding signals. *Trends in cell biology* 28(4):258–273.
2. Clapham DE (2007) Calcium signaling. *Cell* 131(6):1047–1058.
3. Cuthbertson KR, Cobbold P (1985) Phorbol ester and sperm activate mouse oocytes by inducing sustained oscillations in cell Ca^{2+}. *Nature* 316(6028):541.
4. Berridge MJ (2005) Unlocking the secrets of cell signaling. *Annu. Rev. Physiol.* 67:1–21.
5. Orrenius S, Zhivotovsky B, Nicotera P (2003) Calcium: Regulation of cell death: the calcium–apoptosis link. *Nature reviews Molecular cell biology* 4(7):552.
6. Wei C, et al. (2009) Calcium flickers steer cell migration. *Nature* 457(7231):901.
7. Carafoli E (2002) Calcium signaling: a tale for all seasons. *Proceedings of the National Academy of Sciences* 99(3):1115–1122.
8. Martin N, Bernard D (2017) Calcium signaling and cellular senescence. *Cell calcium*.
9. Humeau J, et al. (2017) Calcium signaling and cell cycle: progression or death. *Cell calcium*.
10. La Rovere RM, Roest G, Bultynck G, Parys JB (2016) Intracellular Ca^{2+} signaling and Ca^{2+} microdomains in the control of cell survival, apoptosis and autophagy. *Cell calcium* 60(2):74–87.
11. Parekh AB (2011) Decoding cytosolic Ca^{2+} oscillations. *Trends in biochemical sciences* 36(2):78–87.
12. Ohno Y, Otaki JM (2015) Spontaneous long-range calcium waves in developing butterfly wings. *BMC developmental biology* 15(1):17.
13. Mammano F, Bortolozzi M (2018) Ca^{2+} signaling, apoptosis and autophagy in the developing cochlea: milestones to hearing acquisition. *Cell calcium* 70:117–126.
14. Ceriani F, Pozzan T, Mammano F (2016) Critical role of atp-induced atp release for Ca^{2+} signaling in nonsensory cell networks of the developing cochlea. *Proceedings of the National Academy of Sciences* 113(46):E7194–E7201.
15. Brodskiy PA, et al. (2019) Decoding calcium signaling dynamics during Drosophila wing disc development. *Biophysical journal* 116(4):725–740.
16. Loew LM (2007) Where does all the pip2 come from? *The Journal of physiology* 582(3):945–951.
17. Czech MP (2000) Pip2 and pip3: complex roles at the cell surface. *Cell* 100(6):603–606.
18. Politi A, Gaspers LD, Thomas AP, Höfer T (2006) Models of IP_3 and Ca^{2+} oscillations: frequency encoding and identification of underlying feedbacks. *Biophysical journal* 90(9):3120–3133.
19. Sneyd J, et al. (2017) On the dynamical structure of calcium oscillations. *Proceedings of the National Academy of Sciences* p. 201614613.
20. Dye NA, et al. (2017) Cell dynamics underlying oriented growth of the drosophila imaginal disc. *Development* 144(23):4406–4421.
21. Long J, Deymier PA, Runge K, Hoying JB (2014) Regulation of the frequency and wavelength of calcium waves propagating in networks of interconnected cells: A simulation study. *Trends in Cell & Molecular Biology* 9:19–33.
22. Lloyd S (1982) Least squares quantization in pcm. *IEEE transactions on information theory* 28(2):129–137.
23. Brand AH, Perrimon N (1993) Targeted gene expression as a means of altering cell fates and generating dominant phenotypes. *Development* 118(2):401–415.
24. Duffy JB (2002) Gal4 system in drosophila: a fly geneticist's swiss army knife. *genesis* 34(1-2):1–15.
25. Litosch I (2016) Decoding Gαq signaling. *Life sciences* 152:99–106.
26. Wyss C (1982) Ecdysterone, insulin and fly extract needed for the proliferation of normal drosophila cells in defined medium. *Experimental cell research* 139(2):297–307.
27. Zartman J, Restrepo S, Basler K (2013) A high-throughput template for optimizing drosophila organ culture with response-surface methods. *Development* 140(3):667–674.
28. Hevia CF, López-Varea A, Esteban N, de Celis JF (2017) A search for genes mediating the growth-promoting function of tgfβ in the drosophila melanogaster wing disc. *Genetics* 206(1):231–249.
29. Brogiolo W, et al. (2001) An evolutionarily conserved function of the drosophila insulin receptor and insulin-like peptides in growth control. *Current biology* 11(4):213–221.
30. Xu C, Watras J, Loew LM (2003) Kinetic analysis of receptor-activated phosphoinositide turnover. *The Journal of cell biology* 161(4):779–791.
31. Larkin JW, et al. (2018) Signal percolation within a bacterial community. *Cell systems* 7(2):137–145.
32. Justet C, Hernández JA, Torriglia A, Chifflet S (2016) Fast calcium wave inhibits excessive apoptosis during epithelial wound healing. *Cell and tissue research* 365(2):343–356.
33. Kaouri K, Maini PK, Skourides P, Christodoulou N, Chapman SJ (2019) A simple mechanochemical model for calcium signalling in embryonic epithelial cells. *Journal of mathematical biology* pp. 1–34.
34. Narciso C, et al. (2015) Patterning of wound-induced intercellular Ca^{2+} flashes in a developing epithelium. *Physical biology* 12(5):056005.
35. Narciso CE, Contento NM, Storey TJ, Hoelzle DJ, Zartman JJ (2017) Release of applied mechanical loading stimulates intercellular calcium waves in drosophila wing discs. *Biophysical journal* 113(2):491–501.
36. Held Jr LI (2005) *Imaginal discs: the genetic and cellular logic of pattern formation*. (Cambridge University Press) Vol. 39.
37. Perkins LA, et al. (2015) The transgenic rnai project at harvard medical school: resources and validation. *Genetics* 201(3):843–852.
38. Baumbach J, Xu Y, Hehlert P, Kühnlein RP (2014) Gαq, gγ1 and plc21c control drosophila body fat storage. *Journal of Genetics and Genomics* 41(5):283–292.
39. Werz C, Köhler K, Hafen E, Stocker H (2009) The drosophila sh2b family adaptor lnk acts in parallel to chico in the insulin signaling pathway. *PLoS genetics* 5(8):e1000596.
40. Kakanj P, et al. (2016) Insulin and tor signal in parallel through foxo and s6k to promote epithelial wound healing. *Nature communications* 7:12972.
41. Burnette M, Brito-Robinson T, Li J, Zartman J (2014) An inverse small molecule screen to design a chemically defined medium supporting long-term growth of drosophila cell lines. *Molecular BioSystems* 10(10):2713–2723.

Supplementary Information for

From spikes to intercellular waves: tuning the strength of calcium stimulation modulates organ size control

Ramezan Paravitorghabeh, Dharsan Soundarrajan, Jeremiah J. Zartman

Jeremiah J. Zartman.
E-mail: jzartman@nd.edu

This PDF file includes:

Supplementary text
Figs. S1 to S23
Tables S1 to S2
Captions for Movies S1 to S14
References for SI reference citations

Other supplementary materials for this manuscript include the following:

Movies S1 to S14

Supporting Information Text

Mathematical model formation

Outline. In this supplementary information, we provide a comprehensive hierarchical model of Ca^{2+} signaling. Initially, we describe the Ca^{2+} toolkit model used in the paper at the cellular level. Next, we built a 1D model consisting of a chain of cells connected by gap junctions (GJ's). The purpose of the one-dimensional (1D) model is to uncover the collective spatiotemporal behavior of Ca^{2+} dynamics at the tissue level through the analysis of kymographs. Finally, we built an accurate 2D tissue model that explains necessary and sufficient conditions for each of the spatiotemporal classes of Ca^{2+} signaling patterns. For convenience, most of 2D illustrations of SI figures are associated with supplementary videos in the form of simulation movies.

Baseline Ca^{2+} model. We adapted a a model describing the dynamics of key components of the Ca^{2+} signaling toolkit for individual cells as described in (1). The model consists of four state variables representing the state of components of Ca^{2+} signaling. c, p, s, r denote cytosolic concentration of Ca^{2+}, IP_3 concentration, concentration of Ca^{2+} in Endoplasmic Reticulum (ER) and the fraction of IP_3 receptors that has not been deactivated by Ca^{2+}, respectively. The nominal parameters of the model and their meaning are summarized in Table S1. The dynamics of IP_3 is given by (1)

$$\begin{aligned}
\frac{\partial p}{\partial t} &= D_p \cdot \nabla^2 p + \nu_{\text{PLC}} - \nu_{\text{deg}} \\
&= D_p \cdot \nabla^2 p + \nu_{\text{PLC}} - \nu_{\text{5K}} \\
&= D_p \cdot \nabla^2 p + V_{\text{PLC}} \cdot \frac{c^2}{c^2 + K_{\text{PLC}}^2} - k_{\text{5P}}p
\end{aligned} \tag{1}$$

Here, D_p is the permeability of gap junctions (GJ's) with respect to IP_3. Note that the IP_3 production rate given by the parameter ν_{PLC} refers to production of IP_3 through PLC enzymes (PLC–γ or PLC–β). The parameter ν_{PLC} is Ca^{2+} dependent, and ν_{deg} is the degradation rate.

The dynamics of Ca^{2+} concentrations within the cell cytoplasm is given by

$$\begin{aligned}
\frac{\partial c}{\partial t} &= D_c \cdot \nabla^2 c + \nu_{\text{rel}} - \nu_{\text{serca}} + \nu_{\text{in}} - \nu_{\text{out}} \\
&= D_c \cdot \nabla^2 c + \underbrace{\left[k_1 \left(r \cdot \frac{c}{K_a + c} \frac{p}{K_p + p} \right)^3 + k_2 \right] (s - c)}_{\nu_{\text{rel}}} - \underbrace{V_{\text{serca}} \frac{c^2}{c^2 + K_{\text{serca}}^2}}_{\nu_{\text{serca}}}
\end{aligned} \tag{2}$$

where $\nu_{\text{rel}}, \nu_{\text{serca}}$ refer to release flux from ER and uptake rate to ER by SERCA ATPase, respectively. In this model, the concentration of Ca^{2+} inside ER is governed by

$$\frac{ds}{dt} = \frac{1}{\beta} \left(V_{\text{serca}} \frac{c^2}{c^2 + K_{\text{serca}}^2} - \left[k_1 \left(r \cdot \frac{c}{K_a + c} \frac{p}{K_p + p} \right)^3 + k_2 \right] (s - c) \right), \tag{3}$$

where β is the ratio of cytoplasmic volume to ER volume. Finally, the dynamic of IP_3 inactivation by Ca^{2+} is given by

$$\frac{dr}{dt} = \nu_{\text{rec}} - \nu_{\text{inact}} = \frac{1}{\tau_r} \left(1 - r \frac{K_i + c}{K_i} \right). \tag{4}$$

The nominal values of the parameters and their descriptions in this model are described in Table S1. Note that V_{PLC} is the maximum rate of IP_3 production by PLC within the cell and depends on the agonist concentration, upstream of PLC activation. In this baseline model, increasing V_{PLC} increases the frequency of oscillations and decreases the amplitude of Ca^{2+} signal. Furthermore, V_{PLC} serves as a bifurcation parameter. In nonlinear dynamical systems, a bifurcation parameter refers to a parameter in the system when its value changes slightly, it can cause an abrupt change in the system behavior.

Ramezan Paravitorghabeh, Dharsan Soundarrajan, Jeremiah J. Zartman

Table S1. The parameters and nominal values of the baseline Ca^{2+} toolkit model. The parameters are mostly obtained from (1). See Table I in (1) and references there for more details.

Parameter	Description	Values from (1)
k_{5P}	IP$_3$ dephosphorylation rate	$0.66\,s^{-1}$
K_{PLC}	Half-activation of PLC	$0.2\,\mu M$
V_{PLC}	Maximum production rate of IP$_3$	$1.5\,\mu M s^{-1}$
β	Ratio of effective volumes ER/cytosol	0.185
V_{serca}	Maximum SERCA pump rate	$0.9\,\mu M s^{-1}$
K_{serca}	Half-activation constant	$0.1\,\mu M$
c_{tot}	Total Ca^{2+} concentration in cell	$2\,\mu M$
k_1	Maximum rate of Ca^{2+} release	$1.1\,s^{-1}$
k_2	Ca^{2+} leak	$0.0203\,s^{-1}$
K_a	Ca^{2+} binding to activating site	$0.08\,\mu M$
K_i	Ca^{2+} binding to inhibiting site	$0.4\,\mu M$
K_p	IP$_3$ binding	$0.13\,\mu M$
τ_r	Characteristic time of IP$_3$ receptor inactivation	$12.5\,s$

36 **Single cell model calibration.** For single cell analysis, the diffusion terms are set to be zero. The exact values of the parameters
37 described in Table S1 are unknown in the epithelial cells of wing imaginal discs. However, we used these parameters as initial,
38 baseline parameters. We subsequently modified differential equation describing r in Eq. (4) to match the experimental data.
39 Two important factors that needed to be calibrated were the duty cycle (the fraction of one period which the signal is active)
40 and the frequency of oscillations. Fig. S1 illustrates typical experimental ROI - based Ca^{2+} signal of a wing disc, where the
41 period is in the order 10 minutes and duty cycle is $40-50\%$.
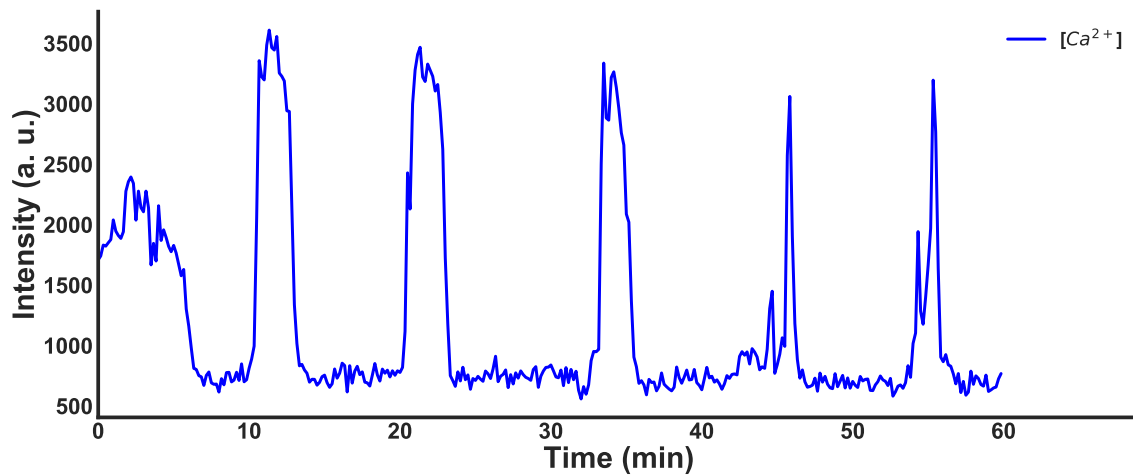

Fig. S1. Experimental data. Agonist stimulated (fly extract concentration 15%) generates oscillatory Ca^{2+} signals in the wing disc system that have relatively long period (in the order 10 minutes) with variable duty cycles. The region of interest selected is the average intensity of four pixels in an experimental image. The signal is the fluorescence intensity of the genetic encoded calcium sensor (GCaMP6) (2).

42 Therefore, we modified the model by scaling the time constant τ_r similar to (3). The new time constant is a function of
43 cytosolic Ca^{2+} as described below,

$$\tau_r(c) \triangleq \tau_{\max} \frac{k_\tau^4}{k_\tau^4 + c^4}. \tag{5}$$

45 Therefore, the new dynamics of r are described by

$$\frac{dr}{dt} = \frac{1}{\tau_{\max}} \frac{k_\tau^4 + c^4}{k_\tau^4} \left(1 - r\frac{K_i + c}{K_i}\right). \tag{6}$$

Furthermore, we assumed that the total Ca^{2+} concentration in a single cell model is fixed (when diffusion is allowed, this assumption is not valid anymore as can be seen in equation 3). For convenience, we summarize equations used for following

single cell analysis below

$$\frac{dc}{dt} = \left[k_1 \left(r \cdot \frac{c}{K_a + c} \frac{p}{K_p + p} \right)^3 + k_2 \right] \left(s - c \right) - V_{\text{serca}} \frac{c^2}{c^2 + K_{\text{serca}}^2} \tag{7}$$

$$\frac{dp}{dt} = V_{\text{PLC}} \cdot \frac{c^2}{c^2 + K_{\text{PLC}}^2} - k_{5\text{P}} p \tag{8}$$

$$s = \frac{c_{\text{tot}} - c}{\beta} \tag{9}$$

$$\frac{dr}{dt} = \frac{1}{\tau_{\max}} \frac{k_\tau^4 + c^4}{k_\tau^4} \left(1 - r \frac{K_i + c}{K_i} \right) \tag{10}$$

47   Nominal values of $\tau_{\max}$ and k_τ are summarized in Table S2. Note that as $k_\tau \to \infty$ or $c \to 0$, the model reduces to the baseline model. However, in the range where $c \gg 0$, k_τ regulates the Ca^{2+} pulse width.

Table S2. Additional parameters and nominal values of the modified Ca^{2+} toolkit model.

Parameter	Description	Baseline values
D_p	GJ permeability for IP$_3$	$0.005 \, \mu m^2 s^{-1}$
D_c	GJ permeability for Ca^{2+}	$0.05 \, \mu m^2 s^{-1}$
$\tau_{\max}$	Maximum time constant of IP$_3$ receptor inactivation	$1000 \, s^{-1}$
k_τ	Ca^{2+} dependent rate of IP$_3$ receptor inactivation	$1 \, \mu M$

48

49   **Simulation details.** For simulations, we used a step size $\Delta t = 0.2 \, s$, final simulation time $T = 3600 \, s$ and sampling time for
50   obtaining kymographs and animations of $10 \, s$. The units of Ca^{2+} and IP$_3$ signals are in μM. These conditions matched the
51   experimental data acquisition rate or were necessary to maintain numerical stability of the simulations.

52   **Properties of the modified model.** As with the baseline model (1), V_{PLC} encodes the maximum production of IP$_3$ and encodes
53   the agonist concentration and is a *Hopf bifurcation* parameter (Fig. S2). Namely, there is a critical threshold on V_{PLC} where
54   the system stability switches and periodic solutions emerge. Fig. S3 demonstrate the change of behavior of Ca^{2+} dynamics
55   in response to stimulus (V_{PLC}). If V_{PLC} is below a threshold $V_{\text{PLC}}^* \approx 0.78$, then there is no oscillations within a window of
56   one simulated hour. However, exceeding the V_{PLC} above the threshold leads to emergence of periodic Ca^{2+} responses. The
57   higher values of V_{PLC} (i) increases the frequency (equivalently, reduces inter-spike intervals) and (ii) reduces the amplitude of
58   Ca^{2+} oscillations. Hence, the encoding of stimulus into Ca^{2+} signals is an amplitude-frequency modulation scheme.

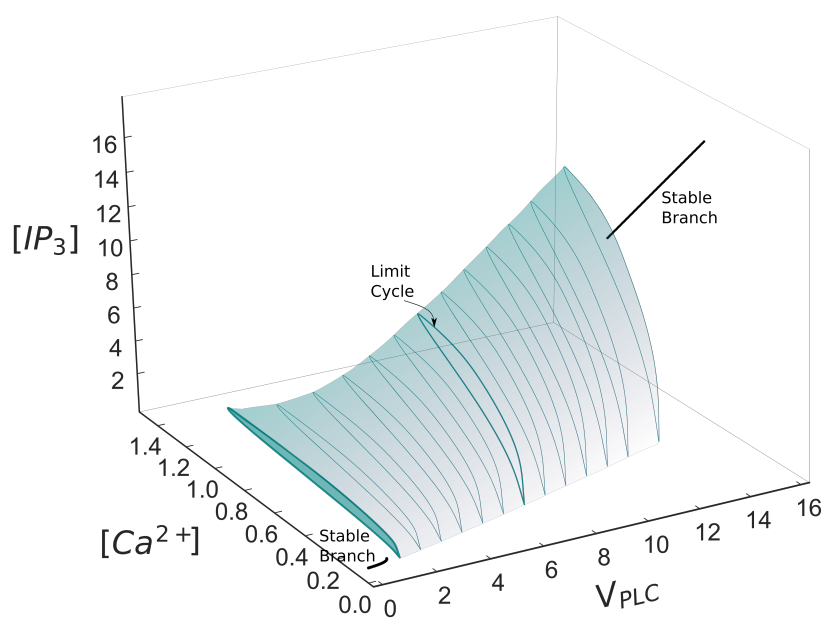**Ramezan Paravitorghabeh, Dharsan Soundarrajan, Jeremiah J. Zartman**

Fig. S2. Bifurcation and phase plane of Ca^{2+} and IP_3 oscillations. Increasing V_{PLC} from 0 to 15. For $0.78 \leq V_{PLC} \leq 11.39$, oscillations arises. The phase plot of Ca^{2+} and IP_3 are shown in colored surface. The stable branches are outside this interval. Simulation parameters are given in Table S1 and Table S2.
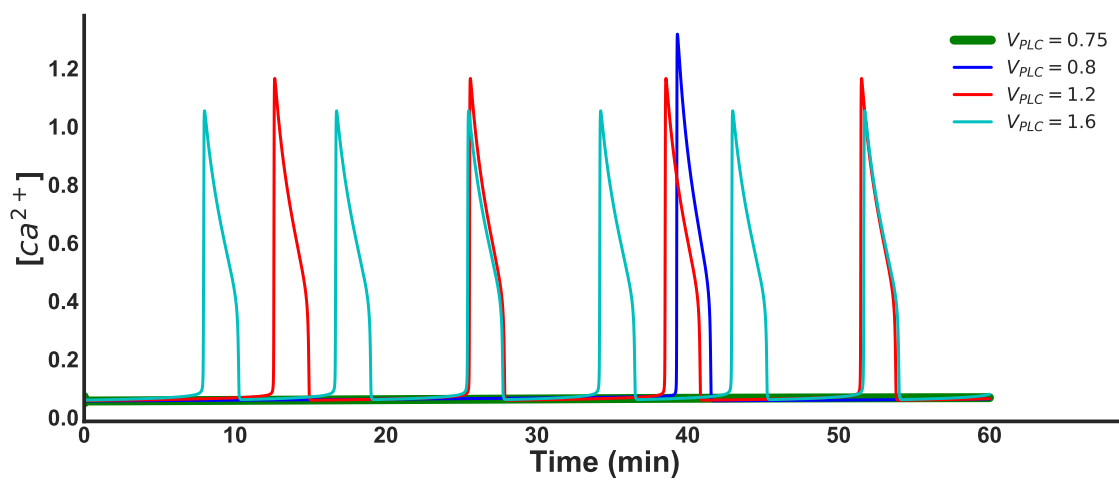
Fig. S3. Amplitude and frequency of oscillations. Single cell Ca^{2+} response in response to stimulus V_{PLC}. Simulation parameters are given in Table S1 and Table S2.

Ramezan Paravitorghabeh, Dharsan Soundarrajan, Jeremiah J. Zartman

59 Another important property of Ca^{2+} signals are the duty cycle (pulse width). In the proposed model, this quantity is
60 controlled by k_τ as depicted in Fig. S4. For fixed amount of $V_{PLC} = 1.2$, the duty cycle increases by increasing k_τ while the
    amplitude remains approximately fixed and frequency decreases.
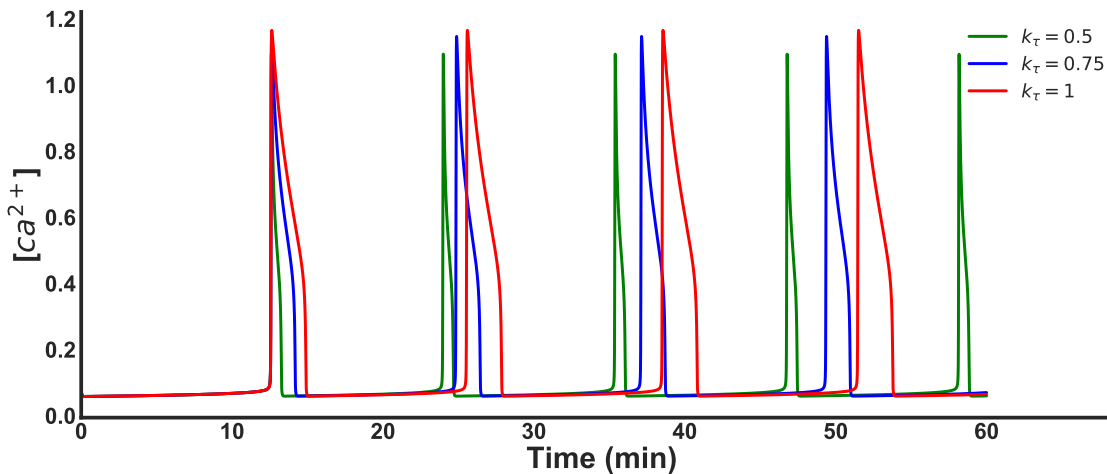
Fig. S4. Duty cycle of oscillations. Increasing k_τ for fixed stimulus $V_{PLC} = 1.2$, increases duty cycle. The parameters are given in Table S1 and Table S2.

61

Supplemental Materials and Methods

Fly stocks

64 A *nub-GAL4, UAS-GCaMP6f* reporter tester line was created by recombining *nub-GAL4* and *UAS-GCaMP6f* lines (4). The
65 final genotype used in all movies is *nub-GAL4, UAS-GCaMP6f/CyO*. Additionally, the tester line was crossed to UAS-*mcherry*
66 to develop another tester line that was used for some imaging experiments. The following UAS-transgene lines were obtained
67 from BDRC: UAS-RyR^{RNAi} (BL#31540), UAS-$InsR^{CA}$ (BL#8248), UAS-$InsR^{DN}$ (BL#8252), UAS-Gq (BL#30734). Progeny
68 wing phenotypes are from F1 male progeny emerging from either nub-Gal4, UAS-GCaMP6f/CyO x UAS-X cross or nub-Gal4,
69 UAS-GCaMP6f/CyO; UAS-mcherry x UAS-X cross. Adult wings were measured using ImageJ and the wing boundaries
70 following vein L1 and L5 respectively. All the flies were raised at 25C andd 12-hour light cycle.

Live imaging

72 Wandering third instar larva approximately 6 days after egg laying was dissected and wing discs were obtained. Wing discs
73 were dissected in ZB media with 15 % fly extract (5). ZB media + 15 % fly extract contains 79.4% (v/v) ZB media, 0.6% (v/v)
74 of 1 mg/ml of insulin (Sigma aldrich), 15% ZB-based fly extract and 5% pennicillin/streptomyocin (Gibco). Wing discs were
75 loaded into previously described REM-Chip (6) and imaged using Nikon Eclipse Ti confocal microscope with a Yokogawa
76 spninning disc and MicroPoint laser ablation system. Image data were collected on an IXonEM+colled CCD camera (Andor
77 technology, South Windsor, CT) using MetaMorph v7.7.9 software (Molecular devices, Sunnyvale, CA). Discs were imaged at
78 three z-planes with a step size of 10 μm, 20x magnification air objective with 10-second intervals for a total period of one hour,
79 with 200 ms exposure time, and 50 nW, 488 nm laser exposure at 44 % laser intensity. We blocked gap junction by inhibiting
80 innexin-2 using Carbenoxolone (Cbx) drug (4). Wing discs were inbulated in ZB + 15% FEX with 30 μM Cbx for one hour
81 before imaging. Cbx was obtained from Sigma aldrich. To induce Ca^{2+} transients, we imaged wing discs in ZB media + 2.5 %
82 FEX. Ca^{2+} waves were induced by imaging the wing disc in ZB media + 15 % FEX and Ca^{2+} fluttering was observed when
83 discs were imaged in ZB media + 40 % FEX respectively.

1D model of intercellular Ca^{2+} signaling

85 We consider a simple chain of cells connected by gap junctions (GJ's) as a basic form of intercellular Ca^{2+} signaling. The
86 purpose of this model is to understand the underlying mechanisms for the formation of spikes, transients and waves. We can
87 think of different forms of Ca^{2+} dynamics as local, short range and long range communication. Therefore, the model provides
88 insight on the role of bifurcation phenomenon in cellular communication. We used kymographs to investigate spatiotemporal
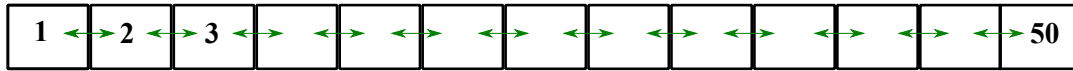89 dynamics under different scenarios as described below.

Fig. S5. Simplified 1D Model. The model consists of 50 cell connected by gap junctions. For simplicity, we assume cells are homogeneous, namely with same parameters as described in Table S1 and Table S2. The green arrows show the direction of gap junction communication. The amount of stimulus applied to cell i is denoted by $V_{\text{PLC}}[i]$, for $1 \leq i \leq 50$.

90 **Permeability of GJ's affect wave speed.** It is known that diffusion of second messengers allow for intercellular communication.
91 Within the context of Ca^{2+} signaling, diffusion of the IP_3 is known to be responsible for propagating communication of
92 Ca^{2+} signal dynamics across tissues . It is assumed that due to buffering of Ca^{2+} , $D_p \gg D_c$. In Fig. S6, we incrementally
93 increase the permeability of GJ's to analyze the effect of D_p. For these simulations, we assume only the first cell is stimulated.
94 When there is no GJ communication, there is no propagation. Increasing D_p causes wave propagation and the speed of waves
95 is proportional to D_p.
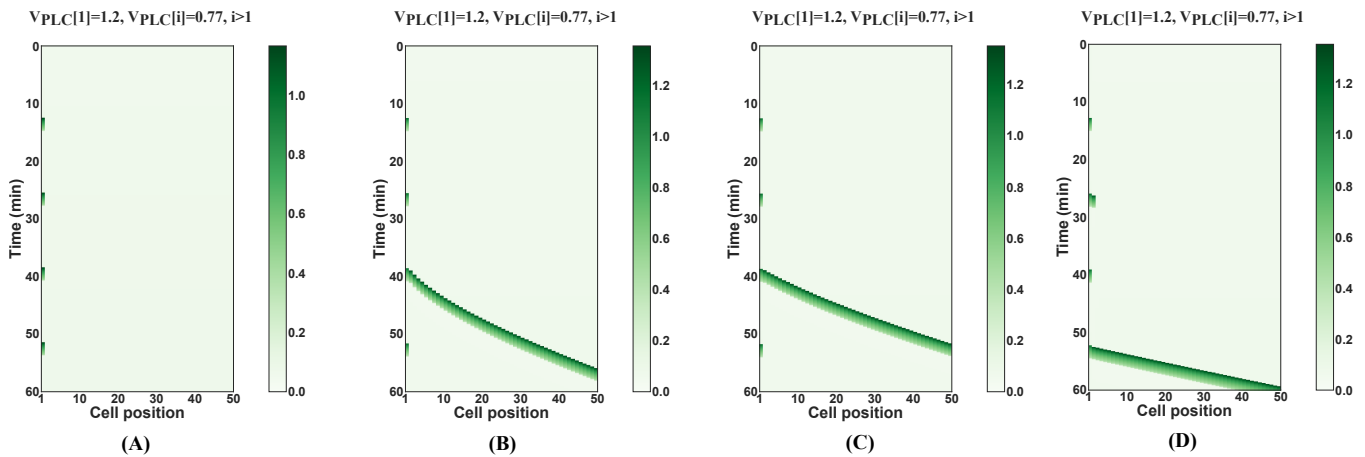
Fig. S6. Effect of GJ permeability. For all panels, the left most cell is stimulated and the rest of the cells are not. The gap junction permeability is varied as follows: (A) $D_p = 0$, $D_c = 0$ (no GJ communication), (B) $D_p = 0.003$, $D_c = 0.005$, (C) $D_p = 0.0005$, $D_c = 0.0005$, (D) $D_p = 0.010$, $D_c = 0.0005$. As it can be seen from the kymographs, the speed of wave propagation increases with increasing D_p. Initial conditions are $c_i = 1, p_i = 1, r_i = .5$ for $1 \leq i \leq 50$.

96 **Waves with limited range.** Intercellular Ca^{2+} transients (ICT's) are a form of dynamics where the range of Ca^{2+} signaling is
97 limited to a couple of cells. Here, we investigate possibilities for such dynamics. One way to get limited range, is to reduce
98 V_{PLC}. In Fig. S7, this effect is depicted by reducing the amount of V_{PLC} in cells (A) 10 and (B) 30, respectively. The range
99 of wave propagation is limited to where the reduction in V_{PLC} happens. **Equivalently, when a collection of cells are**
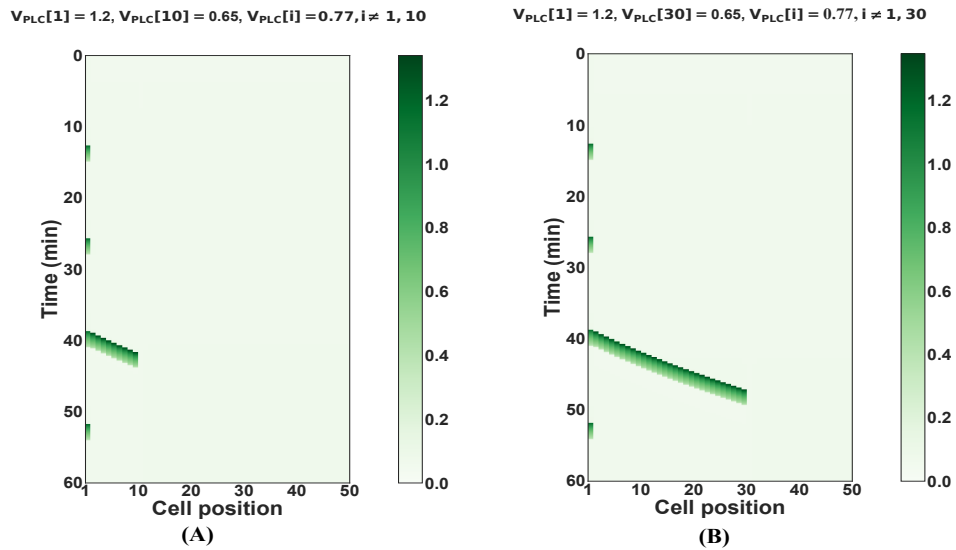100 **stimulated with roughly equal strength near a Hopf bifurcation, wave propagation is facilitated.**

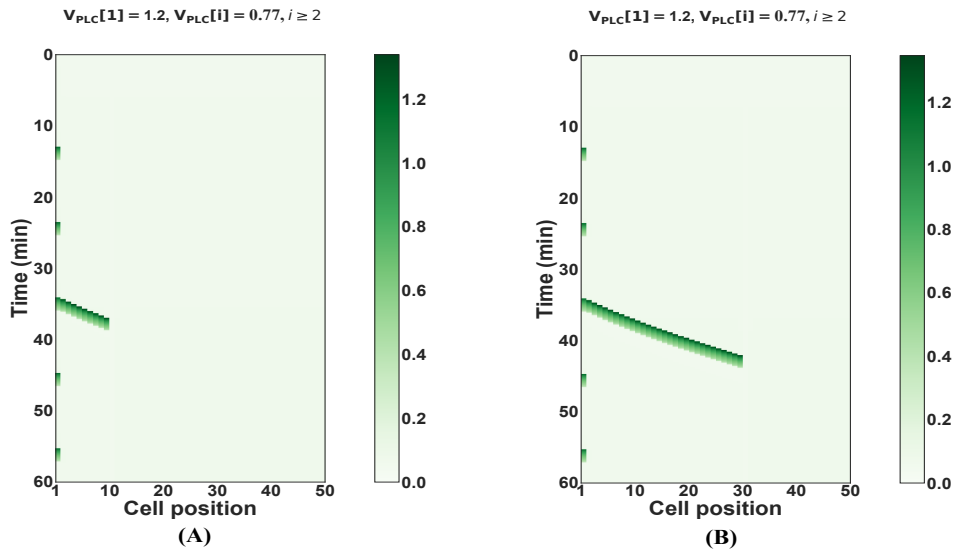**Ramezan Paravitorghabeh, Dharsan Soundarrajan, Jeremiah J. Zartman**

Fig. S7. Waves with limited range (effect of V_{PLC}). For both panels, the left most cell is stimulated and the rest of the cells are not. (A) $V_{\mathrm{PLC}}[10]$ is reduced to 0.65 (B) $V_{\mathrm{PLC}}[30]$ is reduced to 0.65. The other parameters are the same as described in Table S1 and Table S2.

While reducing the V_{PLC} weakens the positive feedback term in the IP$_3$ differential equations, similar effect occurs if degradation rate k_{5P} of IP$_3$ is increased. In Fig. S8, this effect is depicted by increasing the amount of k_{5P} in cells (A) 10 and (B) 30, respectively. Shown in Fig. S8, the range of wave propagation is going to be limited to where the increase in k_{5P} happens.

Fig. S8. Waves with limited range (effect of k_{5P}). For both panels, the left most cell is stimulated and the rest of the cells are not. (A) k_{5P} at cell 10 is increased to 1.5 (B) k_{5P} at cell 30 is increased to 1.5. The other parameters are the same as described in Table S1 and Table S2.

The simulations above demonstrate the important role of IP$_3$ in wave propagation in this model. Specifically, variations in V_{PLC} and k_{5P} have an impact on wave patterning (namely, initiation sites and formation of preferential waves).

Effect of pulse width. The pulse widths of Ca^{2+} signals can be varied by changing k_τ. As it can be seen in Fig. S9, longer pulse widths cause more overlap between signals in consecutive cells.
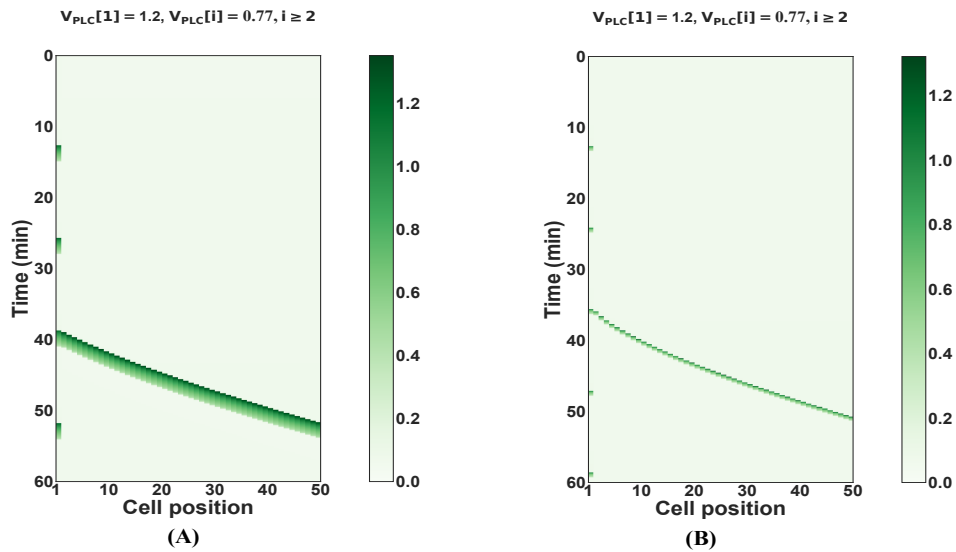
Fig. S9. Effect of pulse width. For all panels, the left most cell is stimulated, and the rest of the cells are not. All cells have (A) $k_\tau = 1$ (B) $k_\tau = .5$. The other parameters are the same as described in Table S1 and Table S2.

Effect of V_{PLC} gradient. The presence of a gradient in V_{PLC} cause variable speeds in wave propagation. As it can be seen in Fig. S10 (A) and (B), in both cases, cells with higher V_{PLC} (left most cells) experience faster Ca^{2+} waves.
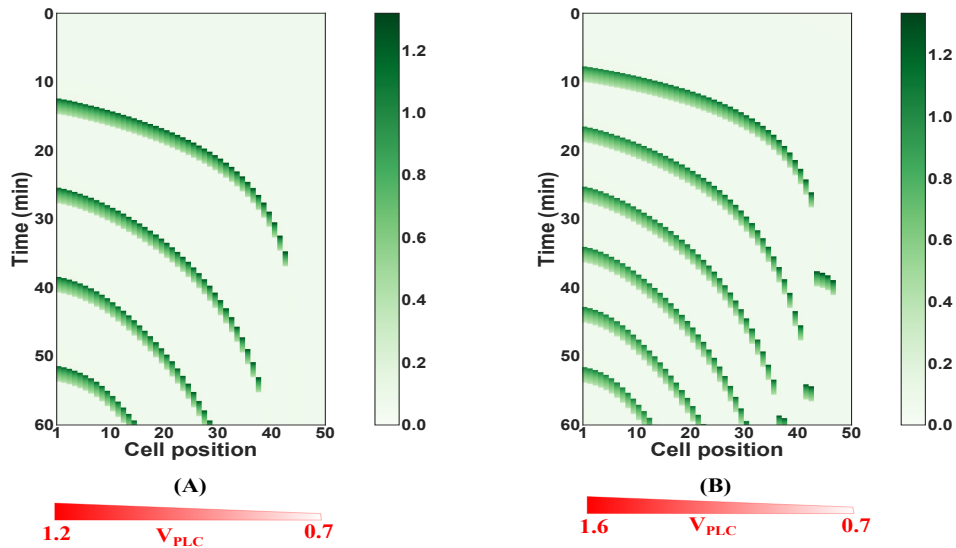

Fig. S10. Effect of V_{PLC} gradient. For all panels, the left most cell is stimulated, and the rest of the cells are not. The value of V_{PLC} have been changed in cells (A) from 1.2 to 0.7, (B) from 1.7 to 0.7. The other parameters are the same as described in Table S1 and Table S2.

What triggers wave propagation? So far, we have considered wave propagation in a deterministic regime, in the sense that the effect of heterogeneity and initial conditions were ignored. Is the diffusion of IP_3 the sole reason for triggering waves? Here, we show that the answer to this question is **negative**. We show that the necessary conditions for triggering waves are **(i) energy content in the diffusive IP_3 pulse, (ii) the fraction of inactive IP_3 receptors must be above a threshold**.

To prove above claims, we performed a series of simulations using the single cell model which reveal the reason behind wave propagation. We modeled external diffusive IP_3 as a square pulse $u_p(t)$ with limited duration, thus the IP_3 dynamics was modified as follows:

$$\frac{dp}{dt} = u_p(t) + \nu_{PLC} - \nu_{deg}. \tag{11}$$

Fig. S11 shows the effect that diffusive IP_3 pulse can cause Ca^{2+} pulses to occur. Fig. S11A shows the lack of dynamics when no external IP_3 diffused. In Fig. S11B-D, the same diffusive pulse is applied at different times denoted by t_0. In (B),

Ramezan Paravitorghabeh, Dharsan Soundarrajan, Jeremiah J. Zartman

there is no Ca^{2+} response, while in (C) and (D) the Ca^{2+} response is triggered. The reason for this is that the activation of positive feedback loop in equation (2) depends on the value of r and p. When r, p are large enough, then the positive feedback loop gets activated.
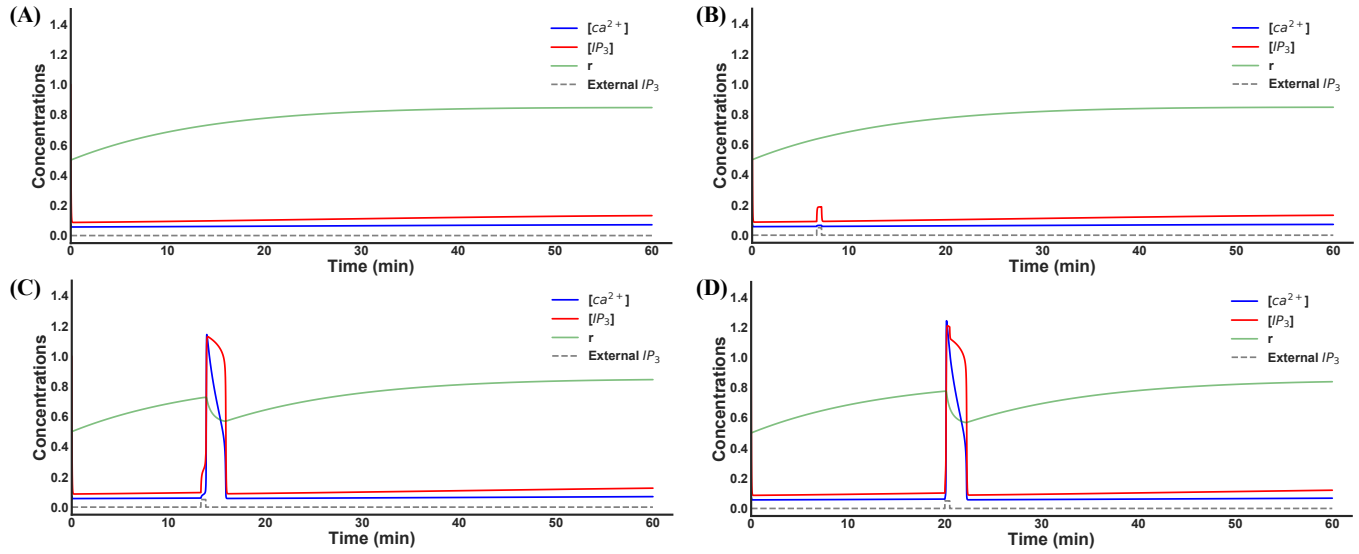

Fig. S11. Triggering mechanism by applying external diffusive IP$_3$. Single cell response by applying diffusive IP$_3$ pulse. For this simulation, $V_{PLC} = 0.77$ and other parameters are the same as described in Table S1. (A) no external IP$_3$, (B) an external IP$_3$ pulse with duration $30s$ and amplitude 0.05 applied at $t_0 = 6$ minutes, (C) an external IP$_3$ pulse with duration $30s$ and amplitude 0.05 applied at $t_0 = 12$ minutes, (D) an external IP$_3$ pulse with duration $30s$ and amplitude 0.05 applied at $t_0 = 20$ minutes. While for (B), (C) and (D) the pulse has the same strength, only in (C) and (D) Ca^{2+} response is induced. This suggests that the fraction of inactivated IP$_3$ receptors r, must be above a threshold to trigger Ca^{2+} response.

The other important factor is the energy of diffusive pulse defined as $\int u_p^2(t)\, dt$. Fig. S12 illustrate this fact by applying diffusive IP$_3$ pulses with different energy levels applied at the same time.
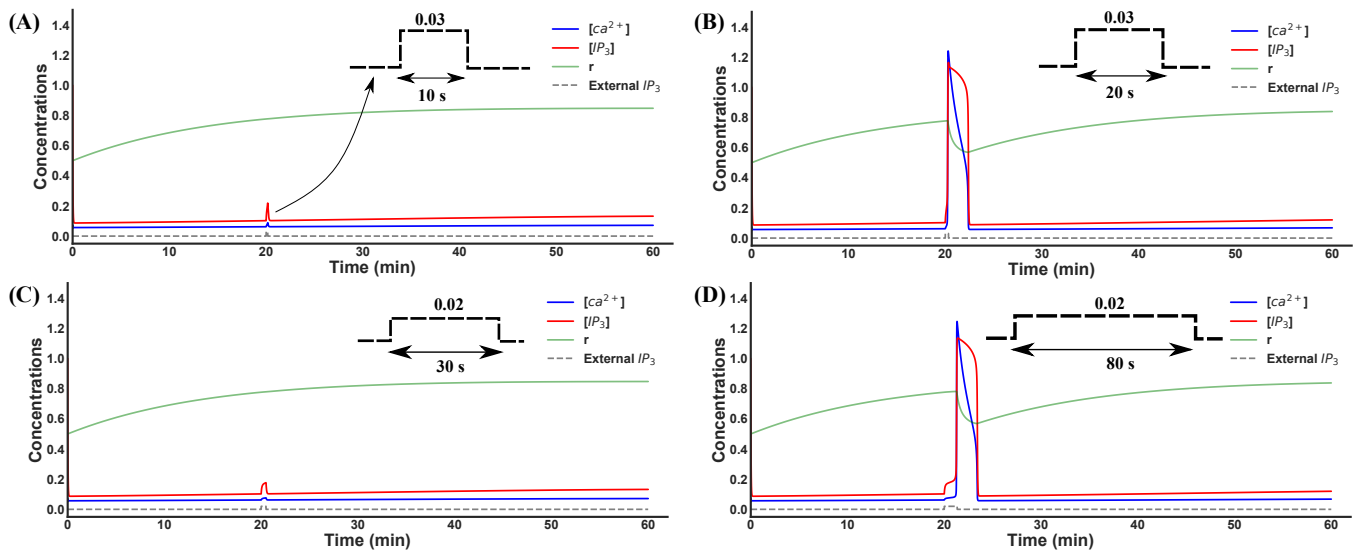
Fig. S12. Energy of external diffusive IP$_3$. Single cell response by applying diffusive IP$_3$ pulse. For this simulation, $V_{\text{PLC}} = 0.77$ and other parameters are the same as described in Table S1. All diffusive IP$_3$ pulses applied at the same time (at 20 minutes) and the shape of pulse is magnified in all panels. (A) no Ca^{2+} response due to weak pulse, (B) Ca^{2+} response is observed by increasing pulse width , (C) no Ca^{2+} response (while the area under curve compared to (C) is fixed), (D) longer pulse width compared to (C) cause Ca^{2+} response. This suggests that the strength of diffusive depends on the overall energy of diffusive IP$_3$ pulse.

The above analysis has following important consequences when studying tissue Ca^{2+} signaling: We can treat the diffusive IP$_3$ signal $u_p(t)$ in the above analysis as the diffusion of IP$_3$ that comes from neighboring cells through GJ's. **Therefore, for Ca^{2+} response to occur in a cell due to diffusion of IP$_3$, not only strength of diffusion matters, but also the state of the cell matters**. Here, the state of the cell refers to r, the fraction of inactivated IP$_3$ receptors. Of course, the permeability of GJ's also affects the strength of diffusion. We elaborate these in the 1D model in the following examples.

Fig. S13 shows an extreme example, the effect of initial value of r. All the cells have the same initial conditions and parameters, except the first cell, which is stimulated. We see the effect of change in initial value of r for cell 25. Depending on the cellular state (defined by variable r here), wave propagation can be stopped or inhibited.
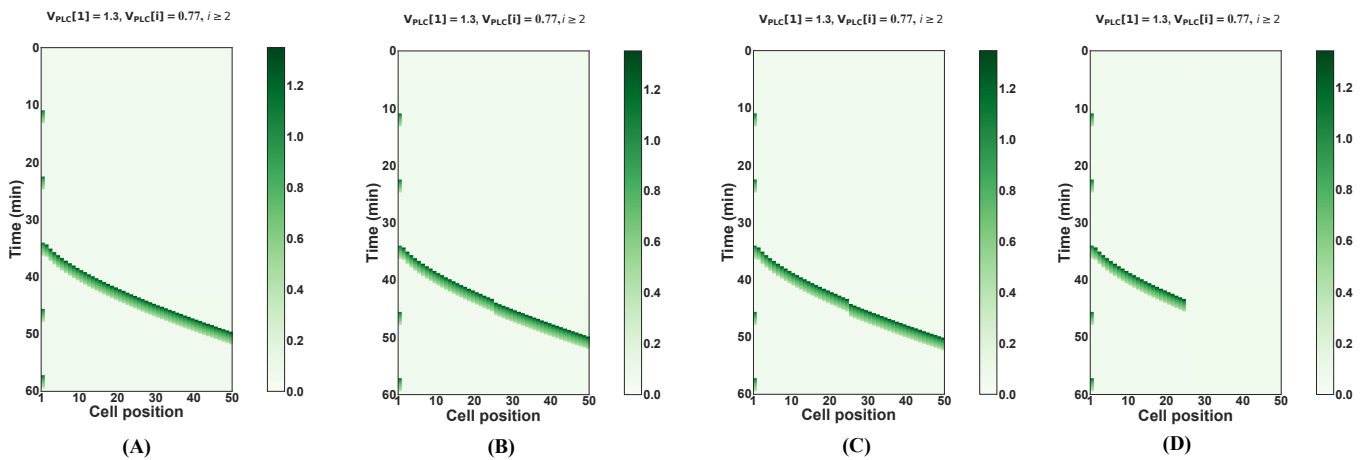

Fig. S13. State of the cells affect wave propagation. For all panels, the left most cell is stimulated and the rest of the cells are not. Initial conditions for r at cell 25 are chosen as (A) 0.5, (B) 0.2, (C) 0.15, (D) 0.1. The other parameters are the same as described in Table S1 and Table S2. In (A), the wave propagates. As it can be seen in (B), (C) and (D), the state of the cell can modify or even inhibit wave propagation. While there is small delay at panels (B) and (C), the wave completely stops in (D).

Formulation of the full 2D tissue-scale model

Building the model. We used experimental images of a wing pouch to model the tissue structure. Figure S14 (a) demonstrates the original image of the epithelia and is overlaid by an elliptical curve representing a region of interest (ROI). We used Icy software and Epitools extension (7, 8) to segment the boundaries of the cells within the tissue restricted to the chosen ROI. The segmentation result is depicted in Figure S14 (b), which encodes information about the tissue structure. The selected ROI in the wing pouch consists of roughly 3225 cells within the ROI.

Ramezan Paravitorghabeh, Dharsan Soundarrajan, Jeremiah J. Zartman

To create a smooth shape for the outer boundaries, we used the convex hull restricted to centroids of the cells. Then, Lloyd's algorithm (9) with four rounds of iterations was used to smoothen the shape of cells. The average number of cell neighbors is 6, which is consistent with literature (see *e.g.* (10)). In terms of diffusion analysis, the length of edges between cells is used as a factor for modeling the strength of chemical communication through the gap junctions. A basic assumption of the model is that gap junctions are homogeneously distributed along the lengths of cell membranes. Fig. S15 shows the final result for the geometry of the tissue.
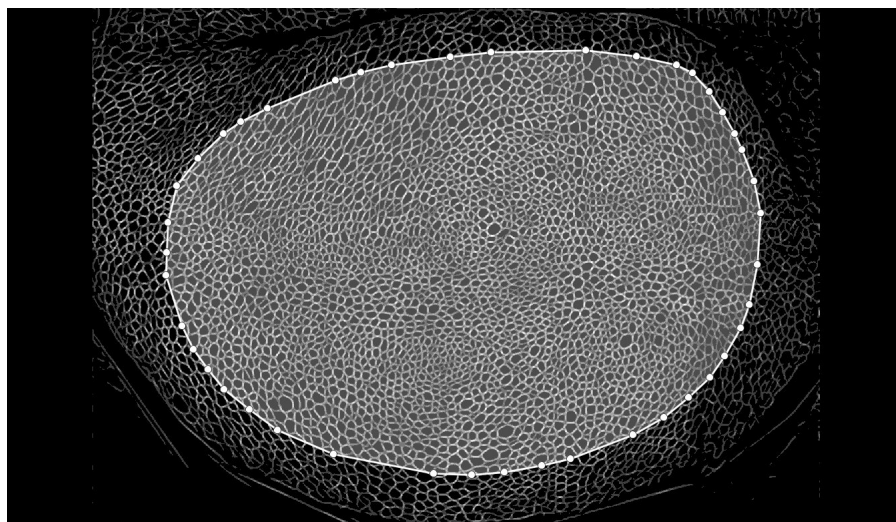
(a)
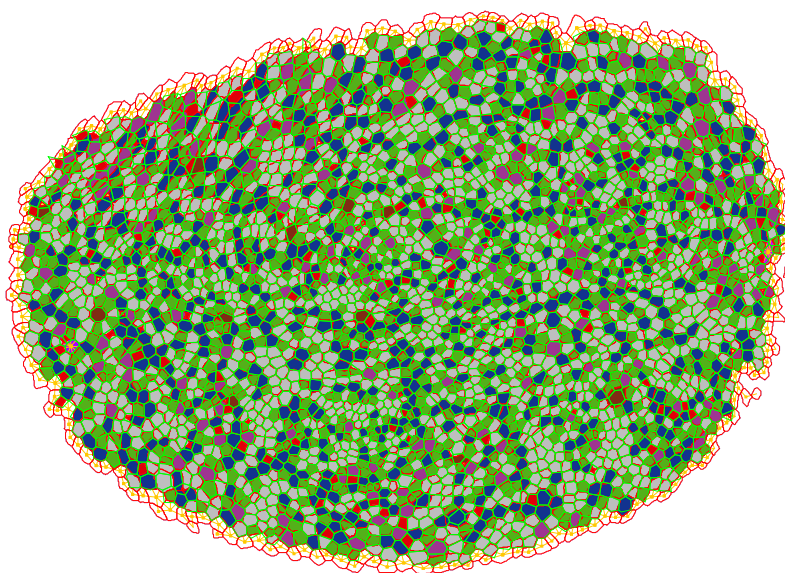
(b)

Fig. S14. (a) The original image of wing pouch and an elliptical region of interest, which is used to segment cell shapes and boundaries. (b) The result of using Epitools for segmentation. The original cell areas are colored based on the number of neighbors. The green edges show result of Voronoi tessellation algorithm applied to centroids of the cells. Cells in the boundary of the tissue are transparent. In the simulations, for those boundary cells, we assume there is no flux along cell membranes that are not shared with other cells.
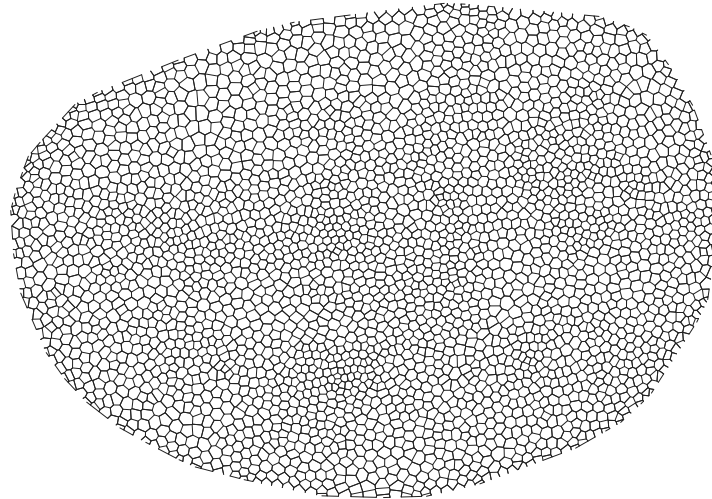
Ramezan Paravitorghabeh, Dharsan Soundarrajan, Jeremiah J. Zartman

Fig. S15. Geometry of the tissue. The final geometric structure of the tissue used for simulating Ca^{2+} signaling. The tissue consists of 3225 cells.

2D simulation details. To simulate Ca^{2+} dynamics at the tissue level, we solved $3225 \times 4 = 12900$ ordinary differential equations (ODE). We assumed individual cells are spatially homogeneous. However, when solving for tissue scale, in addition to a system of ODE's, the diffusion terms are also considered. The diffusive flux of the species such as IP_3 or Ca^{2+} is computed as the weighted difference between a cell and its neighbors. The weights are chosen to be proportional to the length of the edge shared between two neighbors. The permeability coefficient D_p or D_c is based on the parameters given in Table S1. More precisely, if the set of the neighbors of cell i is denoted by $\mathcal{N}(i)$, then the flux corresponding to diffusion term for IP_3 (p) is approximated by

$$\text{Flux} \approx D_p \left[\sum_{j \in \mathcal{N}_i} p_j l_j - p_i \big(\sum_{j \in \mathcal{N}_i} l_j \big) \right] \tag{12}$$

where ℓ_j is the length of the shared edge between cells i and j. Similar rule applies to diffusive Ca^{2+}.

Ca^{2+} spikes when GJ's are blocked. There is no synchronization between cells and individual cell Ca^{2+} levels oscillate independent from each other when the GJ's are blocked. Movie S1 corresponds to the experimental data in this situation:

Movie S1. The experimental data of Ca^{2+} dynamics when the gap junctions are blocked. Wing discs incubated in ZB media with 15 (v/v) % fly extract and 30 μM of Carbonxolene shows uncoordinated Ca^{2+} spikes.

Movie S2. The simulation results of Ca^{2+} dynamics when the gap junctions are blocked. Here, we set $D_p = D_c = 0$. There is no synchronization of Ca^{2+} signals between cells in the tissue.

Ca^{2+} local spikes when GJ's are not blocked. In experimental data, there are local Ca^{2+} spikes despite the presence of GJ communication. Movie S3 corresponds to the experimental data in this situation. Movie S4 depicts the simulation result, which exhibits local spikes. Figure S16 shows the stimulation profile (values of V_{PLC} for individual cells). This simulation suggests that local spikes occur when most of the cell have low V_{PLC}, except for a few cells which have higher levels V_{PLC}. In this case, the spikes occur at those cells despite GJ diffusion. The low amount of V_{PLC} in neighboring cells inhibits propagation of Ca^{2+} waves.

Movie S3. Experimental data for local Ca^{2+} spikes. Third instar wings dissected 7 days after egg laying and dissected in ZB media with 15 (v/v)% fly extract inhibit localized Ca^{2+} spikes

Movie S4. The simulation results of Ca^{2+} local spikes when gap junction-based communication is present.
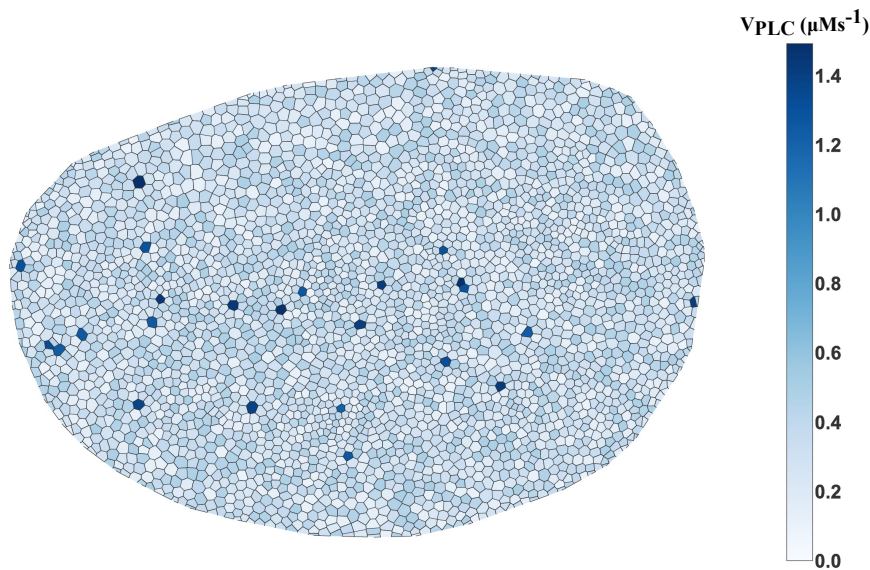
Fig. S16. Stimulation profile for local Ca^{2+} spikes corresponding to Movie S4. This figures illustrates the color map of V_{PLC} throughout the tissue. We assumed V_{PLC} remains fixed throughout simulation interval. Local spikes occur at vicinity of individual cells with high values of stimulation.

Ca^{2+} transients. In experimental data, we observed a class of Ca^{2+} dynamics that resemble waves, but with a very limited propagation range. Movie S5 corresponds to the experimental data in this situation. Movie S6 depicts the simulation result to have transients. Fig. S17 depict the stimulation profile of the cells in this simulation.

Movie S5. Experimental data for Ca^{2+} transients. Third instar wing discs dissected 6 days after egg laying and incubated in ZB media with 15 (v/v) % fly extract results in Ca^{2+} transients.

Movie S6. The simulation results of Ca^{2+} transients associated with V_{PLC} distribution in Fig. S17.
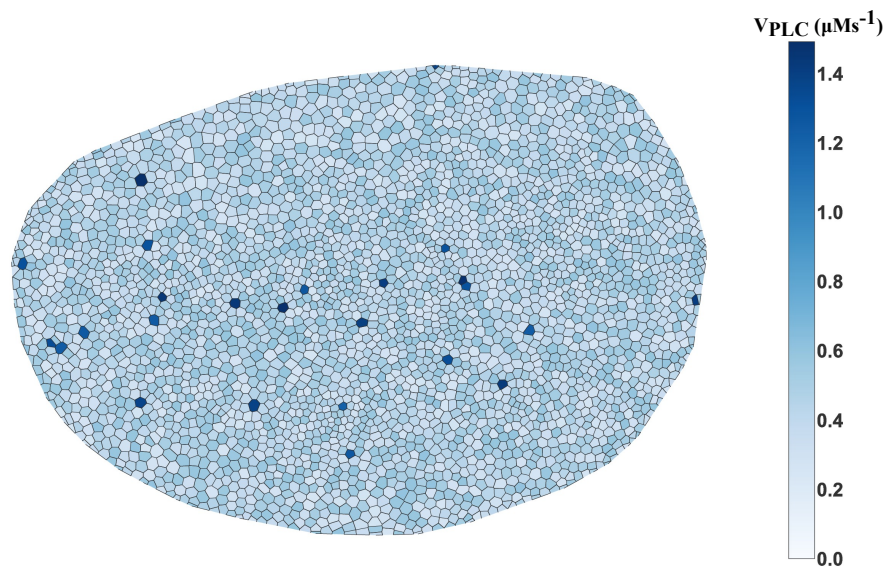

Fig. S17. Stimulation profile for local Ca^{2+} spikes corresponding to Movie S6. This figures illustrates the color map of V_{PLC} throughout the tissue. We assumed V_{PLC} remains fixed throughout simulation interval.

Ca^{2+} waves. The 1D model suggests that the diffusion of IP$_3$ with enough strength can trigger waves spreading throughout the tissue. In this section, we provide the simulation results regarding different wave patterns. We emphasize that the results are based on simplified model of Ca^{2+}. There are multiple factors such as heterogeneity in the set of parameters that were not considered in this study for simplicity.

Ramezan Paravitorghabeh, Dharsan Soundarrajan, Jeremiah J. Zartman

179   The first class of waves occur when the cells are at rest near the Hopf bifurcation and a stimulus is applied to a single cell.
180 This creates a wave which travels throughout the tissue. This scenario is illustrated in Movie S7 and Fig. S18.
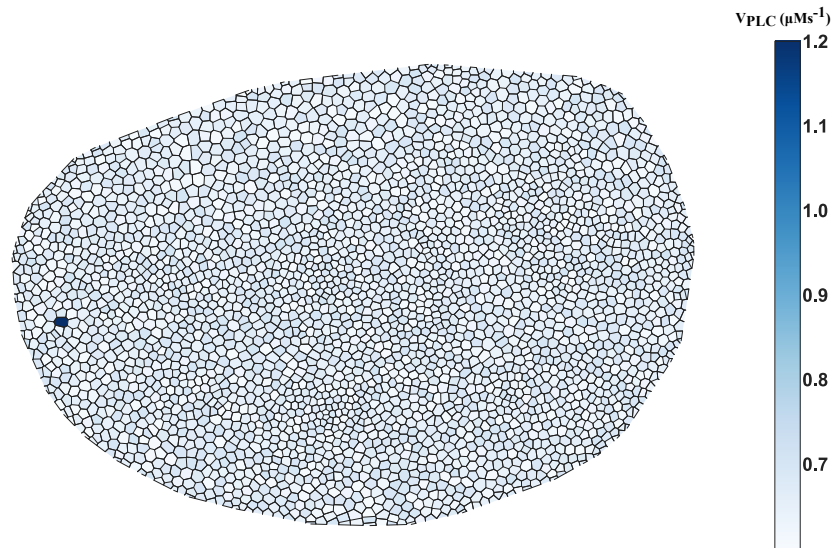181 **Movie S7. The simulation results of stimulating a single cell and obtaining Ca^{2+} waves.**

Fig. S18. Stimulation profile for Ca^{2+} wave corresponding to Movie S7. This figures illustrates the color map of V_{PLC} throughout the tissue. We assumed V_{PLC} remains fixed throughout simulation interval. A single cell is stimulated by setting high value for its $V_{\text{PLC}} = 1.2$. The rest of cells have random uniform $V_{\text{PLC}} \in [0.6, 0.7]$ which is below the bifurcation threshold.

182   Next we considered the case where the V_{PLC} profile is mostly closed to the Hopf bifurcation, except a tiny fraction of cells,
183 which are initiation sites and have higher V_{PLC}. This scenario is illustrated in Movie S8 and Fig. S19.
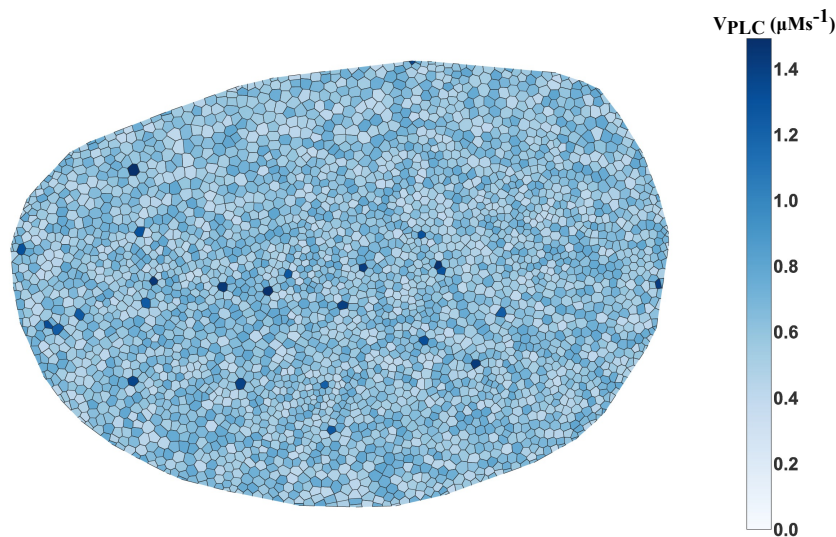184 **Movie S8. The simulation results of randomly stimulating cells and obtaining Ca^{2+} waves.**

Fig. S19. Stimulation profile for Ca^{2+} wave corresponding to Movie S8. This figures illustrates the color map of V_{PLC} throughout the tissue. We assumed V_{PLC} remains fixed throughout simulation interval.

185 **Preferential Ca^{2+} waves.** Preferential waves are the waves which travel in a specific direction. The simulation results suggests
186 that reducing V_{PLC} or increasing IP$_3$ degradation rate within specific regions in the disc inhibits waves to pass those regions.
187 This effect, in return, causes the formation of waves which prefer specific directions. For instance, the experimental data as in
188 Movie S9 demonstrate an instance of radial pattern in Ca^{2+} wave in the imaginal wing disc. By choosing V_{PLC} as depicted in
189 Fig. S20, we see preferential waves.

190   Another example is depicted in Movie S11 where cells in stripe along the anterior/posterior (A/P) and dorsal/ventral (D/V)
191   have smaller values of V_{PLC} as in Fig. S21. The waves in this scenario tend to annihilate along A/P and D/V axes.

192   **Movie S9.**   **Experimental data for radial Ca^{2+} pattern.**

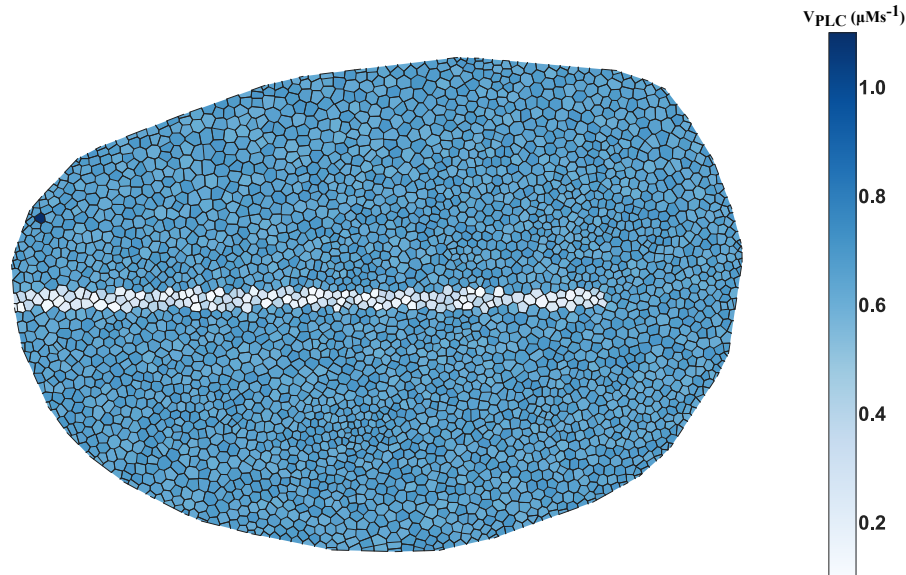193   **Movie S10.**   **The simulation results of radial Ca^{2+} pattern.**

Fig. S20. Stimulation profile for Ca^{2+} wave radial pattern corresponding to Movie S10. This figures illustrates the color map of V_{PLC} throughout the tissue. We assumed V_{PLC} remains fixed throughout simulation interval. A single cell is stimulated by setting high value for its $V_{\mathrm{PLC}} = 1.1$. A stripe of cells along A/P axis is chosen to have very low V_{PLC}. The rest of cells have random uniform $V_{\mathrm{PLC}} \in [0.6, 0.7]$ which is below the bifurcation threshold.

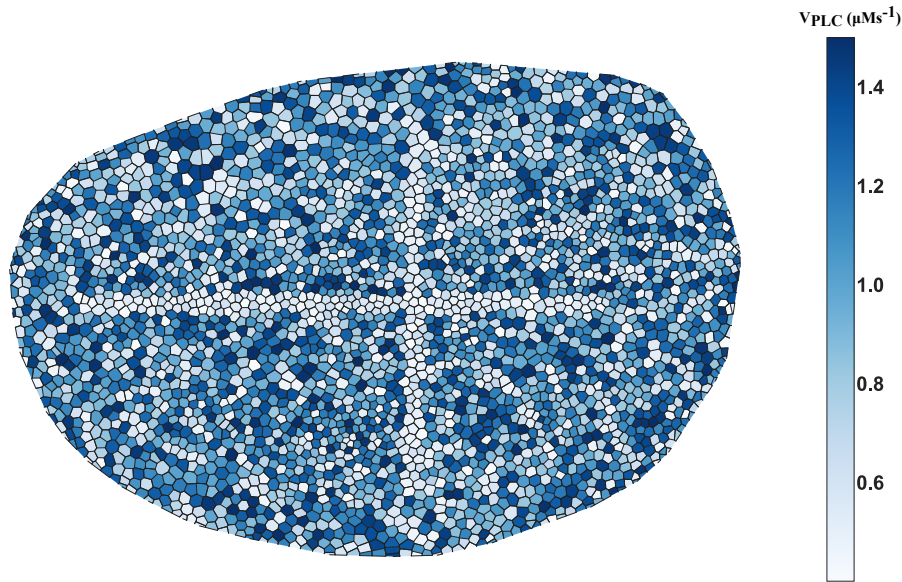194   **Movie S11.**   **The simulation results of preferential Ca^{2+} waves with random stimulation.**

Ramezan Paravitorghabeh, Dharsan Soundarrajan, Jeremiah J. Zartman

Fig. S21. Stimulation profile for Ca^{2+} preferential pattern corresponding to Movie S11. This figures illustrates the color map of V_{PLC} throughout the tissue. We assumed V_{PLC} remains fixed throughout simulation interval. A stripe of cells along A/P and D/V axis is chosen to have relatively low V_{PLC}. The rest of cells have random uniform $V_{PLC} \in [0.3, 1.2]$.

Fluttering pattern. The final class of experimental Ca^{2+} dynamics is the fluttering pattern where the whole disc is in an active signaling state. Movie S12 and Movie S13 correspond to experimental and simulation results. In simulations, all cell have chosen to have high V_{PLC}. However, the other important factor which cause fluttering to occur is higher values of K_{serca}. Fig. S23 depicts a typical signal in fluttering mode. Note that compared to Fig. S3, the oscillations occur around a higher basal level.

Movie S12. Experimental data for the fluttering state. Third instar wing discs incubated in ZB media + 40 (v/v) % fly extract shows Ca^{2+} fluttering

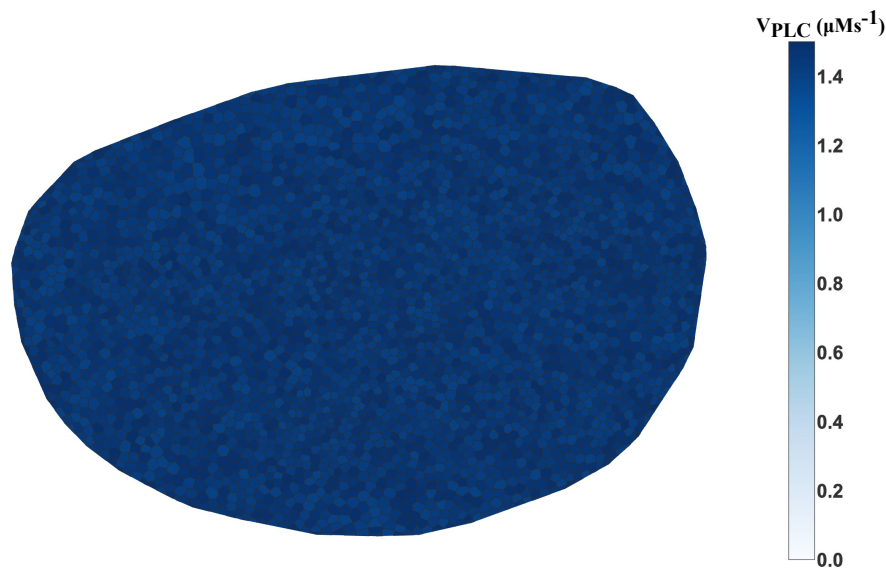**Movie S13. The simulation result for fluttering effect.**

Fig. S22. Stimulation profile of fluttering case corresponding to Movie S13. This figures illustrates the color map of V_{PLC} throughout the tissue. We assumed V_{PLC} remains fixed throughout simulation interval.

Ramezan Paravitorghabeh, Dharsan Soundarrajan, Jeremiah J. Zartman
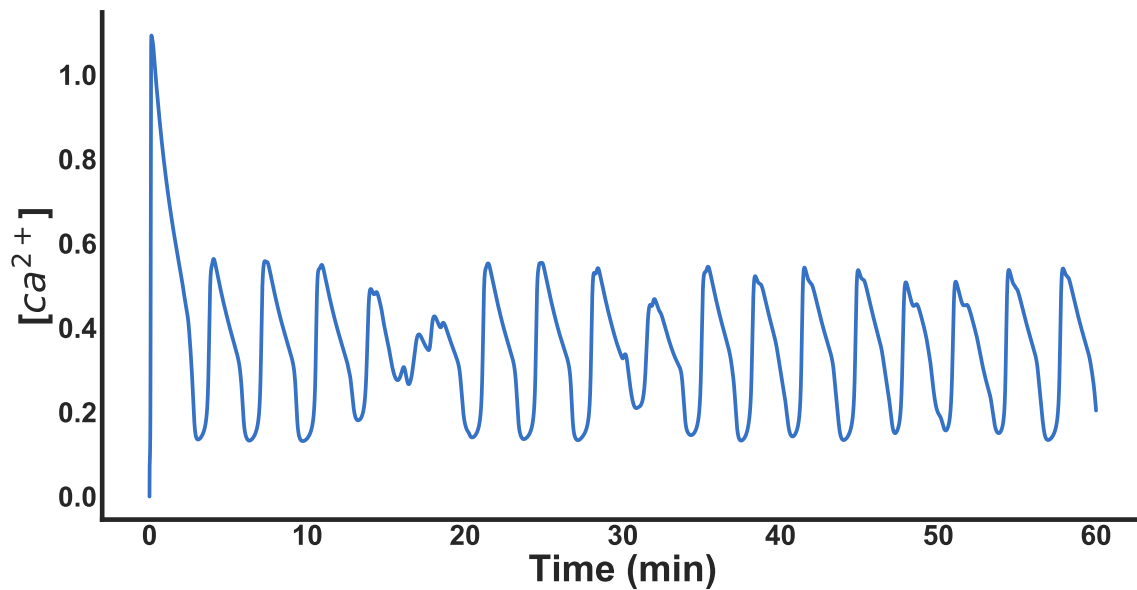
Fig. S23. Typyical form of Ca²⁺ fluttering signal. The fluttering signal oscillate around an elevated basal level.

203 **Movie S14.** The overexpression of $\mathrm{G}-\alpha q$ induces Ca^{2+} waves.

References

205 1. Politi A, Gaspers LD, Thomas AP, Höfer T (2006) Models of ip3 and Ca²⁺ oscillations: frequency encoding and
206   identification of underlying feedbacks. *Biophysical journal* 90(9):3120–3133.
207 2. Brodskiy PA, et al. (2019) Decoding calcium signaling dynamics during Drosophila wing disc development. *Biophysical*
208   *journal* 116(4):725–740.
209 3. Sneyd J, et al. (2017) On the dynamical structure of calcium oscillations. *Proceedings of the National Academy of Sciences*
210   p. 201614613.
211 4. Narciso C, et al. (2015) Patterning of wound-induced intercellular Ca²⁺ flashes in a developing epithelium. *Physical*
212   *biology* 12(5):056005.
213 5. Burnette M, Brito-Robinson T, Li J, Zartman J (2014) An inverse small molecule screen to design a chemically defined
214   medium supporting long-term growth of drosophila cell lines. *Molecular BioSystems* 10(10):2713–2723.
215 6. Narciso CE, Contento NM, Storey TJ, Hoelzle DJ, Zartman JJ (2017) Release of applied mechanical loading stimulates
216   intercellular calcium waves in drosophila wing discs. *Biophysical journal* 113(2):491–501.
217 7. Heller D, et al. (2016) Epitools: an open-source image analysis toolkit for quantifying epithelial growth dynamics.
218   *Developmental cell* 36(1):103–116.
219 8. De Chaumont F, et al. (2012) Icy: an open bioimage informatics platform for extended reproducible research. *Nature*
220   *methods* 9(7):690.
221 9. Lloyd S (1982) Least squares quantization in pcm. *IEEE transactions on information theory* 28(2):129–137.
222 10. Nematbakhsh A, et al. (2017) Multi-scale computational study of the mechanical regulation of cell mitotic rounding in
223   epithelia. *PLoS computational biology* 13(5):e1005533.